Feature Article

Nanostructure development in multicomponent polymer systems characterized by synchrotron X-ray scattering ☆

Nadya Dencheva [a], Almut Stribeck [b], Zlatan Denchev [a,*]

[a] Institute for Polymers and Composites/I3N, University of Minho, 4800-058 Guimarães, Portugal
[b] Institute of Technical and Macromolecular Chemistry, University of Hamburg, Germany

ARTICLE INFO

ABSTRACT

Modern synchrotron beamlines equipped with two-dimensional detectors and high-flux microfocus devices offer interesting possibilities for polymer characterization. This work presents three synchrotron X-ray studies performed in specific multicomponent polymer systems. In the first study, quantification of transcrystallinity in microfibrillar composites (MFC) by wide-angle X-ray scattering (WAXS) and a direct relation between the mechanical properties of the composites and the thickness of the transcrystalline layers is presented. The second study demonstrates monitoring of nanostructure development under controlled strain in MFC and their precursors by small-angle X-ray scattering (SAXS). A specially developed procedure for data treatment that uses the Chord Distribution Function formalism permitted to prove reversible strain-induced crystallization of matrix material in the MFC materials. In the third study, a 5×5 μm high flux X-ray beam was used to scan in WAXS mode polymer microcapsules (average diameters of 20–50 μm) with polyamide shells in which various solid payloads were incorporated by in-situ polymerization. Exfoliation/intercalation phenomena and local inhomogeneity at micron scale are studied in clay and metal containing polyamide microcapsules that constitute a new platform for the development of polymer hybrids or smart micro devices. It was concluded that relating microscopy and/or mechanical data of various polymer samples to their synchrotron WAXS/SAXS patterns helps to understand the structure–properties relationship in complex polymer systems with controlled composition, morphology and nanostructure.

© 2016 Elsevier Ltd. All rights reserved.

Contents

☆ The content of this article was orally presented in September 2015 at the Synchrotron Radiation in Polymer Science Conference (SRPS-6) in Madrid, Spain.
* Corresponding author.
  E-mail address: denchev@dep.uminho.pt (Z. Denchev).

1. Introduction

Nowadays a great number of polymer systems with industrial importance *e.g.,* blends, colloidal polymers, polymer composites or filled polymers, polymer alloys, polymer micro- and nanocapsules *etc.* comprise significant amounts of two or more chemically distinct components. By 2002, the production of multicomponent polymer systems had reached 65% of the total volume of polymer production [1]. A large window has opened for new applications of these systems with the broad introduction of nanotechnologies in polymer science. Changing the type, size, shape, volume fraction, interface, and degree of dispersion or aggregation of the different components enables great amount of unique combinations of properties with high potential for successful commercial development [2]. The wide use of multicomponent polymeric products fostered the investigations on their structure development during processing and the establishment of structure–properties relationships [3,4]. Apart from their industrial importance, the multicomponent materials are model systems in statistical physics for studying fundamental aspects of many properties such as conformational properties of the chains, the kinetics of phase transitions, as well as the detailed dynamics of diffusion processes [5]. The large molecular dimension of polymer systems markedly reduces the mixing entropy and provides the basis for self-organized structures [6]. Hence, investigating polymer systems comprising two or more components has become an important issue within the modern materials science.

Generally, analytical methods involving X-ray scattering are being used for non-destructive structural investigations in polymers in different forms and levels of sophistication for more than 60 years. These methods are a useful tool to study a multicomponent system since they are sensitive to spatial inhomogeneity due to composition or phase fluctuations in polymer materials, either amorphous or semicrystalline. Many relevant studies in this field have been performed by means of small-angle scattering of X-rays (SAXS) or of neutrons (SANS) [7]. The latter technique is less accessible due to the necessity of nuclear reactors and special safety precautions. The wide angle scattering of X-rays (WAXS) called also X-ray diffraction is very frequently used in characterization of semicrystalline systems. The diffraction pattern contains information specific to each phase within the irradiated volume, including both geometric and structural parameters, many of which are inaccessible to other techniques. It is a common feature of all scattering methods that the structural information can be collected non-invasively, providing *in-situ* and real time possibilities, as well as simultaneous application of several analytical techniques. These capabilities turn WAXS and SAXS into powerful tools for structural investigation. Their output can be considerably enhanced by collecting data in synchrotron beamlines [8].

Along with WAXS and SAXS, scanning electron microscopy (SEM) and transmission electron microscopy (TEM) are also extremely useful for structure characterization of multicomponent materials down to the atomic scale. The biggest advantage of the microscopy techniques is the direct observation (*i.e.,* without significant data processing) of real-space images produced by the electrons scattered off of the sample surface (SEM), or by the transmitted electron beam (TEM). Collection of the characteristic X-rays that are generated in the samples in both SEM and TEM by attachments for energy dispersive X-ray analysis (EDX) allow for compositional studies in selected sample domains, as well as obtaining electron diffraction patterns that can be analyzed similarly to WAXS data. The biggest shortcomings of SEM and TEM are the quite complex sample preparation, and the impossibility to follow the structure evolution in dynamic conditions, *e.g.,* under cyclic or continuous strain. Moreover, the SEM and TEM images provide information about a very small area that may not be representative for the sample. At the same time, WAXS and SAXS techniques require no or very little sample preparation and can be used simultaneously with other analytical methods (*e.g.,* mechanical testing [9], calorimetry [10], or dielectric spectroscopy [11,12], *etc.*). Depending on the X-ray beam size, specific sample areas can be irradiated integrating the analytical information over it. On the negative side, X-ray techniques produce information in the reciprocal space that may require relatively complex data processing to extract the structural information. All these features make electron microscopy and X-ray scattering useful complements to each other.

The scope of the present article is limited to three studies on the application of synchrotron X-ray techniques in two particular multicomponent polymer systems. The first system comprises microfibrillar reinforced composites (MFC) produced from oriented blends of thermoplastic semicrystalline polymers. The MFC belong to fiber-reinforced composites that have many important engineering applications but are notoriously difficult to study by X-rays [13]. Static WAXS measurements focusing on the transcrystallization phenomena or SAXS under strain test focusing on crystalline structure development in MFC were performed suggesting new procedures for data handling. As a second material system differently loaded, polyamide 6 based microcapsules (PAMC) produced by *in-situ* polymerization are studied by high flux X-ray beam using WAXS. These powder materials represent a new platform for the development of polymer hybrids and smart microdevices. A setup and a procedure are described for studying the exfoliation/intercalation phenomena and local inhomogeneity in various loaded PAMC systems. The X-ray data from the three studies are discussed in relation to microscopy and/or mechanical data, trying to understand the structure–properties relationship.

2. Experimental

2.1. General description of MFC

The conventional strategy for the production of fiber reinforced polymer composites is the introduction of strong fibers into a bulk polymer matrix [14]. The search for more environmentally friendly polymer composites led to the *in-situ* preparation of both matrix and reinforcing fibers from oriented polymer blends, which resulted in what was called "microfibrillar composites" or MFC [15,16]. These composites are obtained from properly chosen blends of thermoplastic polymers by a combination of mechanical and thermal treatments in three processing stages: (i) melt blending of the starting polymers, (ii) cold drawing of the blend followed by (iii) its selective isotropization at $T_1 < T < T_2$, where T_1 is the melting temperature of the lower-melting, matrix-forming component and T_2 is that of the higher melting one, from which the reinforcing fibrils originate. Since the MFC concept does not employ direct mixing of polymers with fibers, two major problems are resolved, namely achieving proper dispersion of the reinforcing entities and not allowing their aggregation during processing [17]. The diameters of the reinforcing fibrils in MFC are typically bigger than 100 nm and can reach a few microns, so these materials are considered as intermediate between the conventional composites and the nanocomposites [18]. In this study as matrix-forming component high-density polyethylene (HDPE) was used and for the fibril forming component – either polyamide 6 (PA6) or polyamide 12 (PA12). In selected systems a commercial compatibilizer Yparex 8102 (YP, by DSM, The Netherlands) was employed. Additional reinforcement of the MFC microfibrils with nanoclays was tried as a way toward better mechanical properties.

2.2. General description of PAMC

Polyamide powders with micron-sized particles are of demand in various processing procedures, *e.g.,* flame spraying, electrostatic coating, compression- and rotational molding [19–22]. In bioengineering, finely divided polyamide particles are attractive carriers for protein or enzyme immobilization with applications in solid-phase diagnostics, biosensors, biocatalysts, and bio-separation [23–25]. Polymer particles with magnetic or conductive loads may become interesting in applications requiring stimuli responsiveness [26,27]. Neat polyamide microparticles can be prepared by activated anionic ring-opening polymerization (AAP) of lactams in hydrocarbon solutions [19,20,28–30]. Recently, differently loaded PA6 microcapsules (PAMC) were prepared in that way and studied [31]. The present study reports on the use of microfocus WAXS from synchrotron for accessing the microgradients in differently loaded PAMC.

2.3. Materials

In the studied MFC materials the matrix was always formed by the same high-density polyethylene (HDPE). It is produced by Borealis and has a density ρ = 0.952 g/cm^3, melting point (DSC) T_m^{DSC} = 133 °C, average molecular weights $\overline{M}_n$ = 49 kg/mol and $\overline{M}_w$ = 203.1 kg/mol. As fibril-forming minor component either PA6 or PA12 were used. The PA6 granulate is made by Lanxess (ρ = 1.14 g/cm^3, T_m^{DSC} = 220 °C, $\overline{M}_n$ = 76.5 kg/mol, $\overline{M}_w$ = 142.3 kg/mol). The PA12 is the high-viscosity grade Grilamid L 25 of EMS-Grivory (ρ = 1.01 g/cm^3, T_m^{DSC} = 178 °C, with $\overline{M}_n$ = 73.3 kg/mol, $\overline{M}_w$ = 131.9 kg/mol). The compatibilizer Yparex 8102 (YP) made by DSM is a copolymer of linear low-density polyethylene and maleic anhydride (ρ = 0.923 g/cm^3, T_m^{DSC} = 125 °C, with $\overline{M}_n$ = 32 kg/mol, $\overline{M}_w$ = 196.5 kg/mol). The maleic anhydride content of YP is 0.5–1.0 wt% as determined by infrared spectroscopy [32].

For the PAMC preparation by AAP, ε-caprolactam monomer (ECL) of reduced moisture (AP-Nylon®) was delivered from Brüggemann Chemical, Germany. Before use, it was kept under vacuum for 1 h at 50 °C. As AAP activator, Brüggolen C20® from Brüggemann Chemical, Germany (C20) was used. According to the manufacturer, it contains 80 wt% of blocked di-isocyanate in ECL. The initiator sodium dicaprolactamato-bis-(2-methoxyethoxo)-aluminate (80 wt% in toluene) was purchased from Katchem, Czech Republic, and used without further treatment (Dilactamate®, DL). Graphite (GR) powder (platelet size < 1 μm), metal and metal oxide powders were purchased from Sigma Aldrich with >99% purity and grain sizes

varying between 300 and 1500 nm. The solvents used for PAMC preparation are of "puriss" grade purchased from Sigma–Aldrich and were used as received. Two commercial nanoclay brands based on organically treated natural montmorillonite (MMT) were employed in both MFC and PAMC. The Nanomer I.24 TL (NM) is a product of Nanocore Corporation (IL, USA) with 12-aminododecanoic acid as surfactant, the typical aspect ratio of the monolayers being of 200–400, with a maximum moisture content of 3% and cation exchange capacity (CEC) of 135 meq/100 g. The Cloisite 15A clay was delivered by Southern Clay Products (TX, USA) and represent MMT modified by dimethyl dihydrogenated tallow quaternary ammonium chloride and contained up to 2% of moisture, CEC value of 125 meq/100 g, and organic content of 43%. The aspect ratio of the monolayers in the CL15A was reported to be in the 75–100 range [33]. All powdered filler materials were dried for 12 h at 80 °C under slight vacuum before being applied for MFC or PAMC preparation.

2.4. Preparation of oriented precursors for MFC

Granulates of HDPE, PA6 or PA12, and YP, all dried at 100 °C for 6 h, were premixed in the following proportions (wt%): HDPE/PA/YP = 80/20/0; 77.5/20/2.5; 75/20/5, 70/20/10; 65/30/5. For the production of the oriented blend precursors (OP) an extruder line with cold drawing was used, comprising a twin-screw extruder, two water baths, three haul-off devices, a hot air oven and multiaxes winder block [32,34]. The resulting extrudate was cooled in the first water bath. The first haul-off unit applied a slight drawing in order to stabilize the line velocity and the extrudate cross-section. Further drawing was performed in the second and third haul-off units, after heating the extruded strand in the second water bath at 98–99 °C. As a result of this cold drawing, the diameters of the extruded strands decreased from 2.0 mm to 0.6–0.7 mm. At the exit of the last haul-off unit the HDPE/PA/YP blends were obtained in the form of oriented, continuous cables. The latter were cut into bristles with equal length of ca. 20 cm. For the clay-containing oriented precursors (OPs), instead of neat PA6, weighed amounts of previously prepared by extruder blending PA6-MMT pellets were used, maintaining the rest of the processing procedure the same.

2.5. Preparation of the MFCs

Bundles of precursor bristles with unidirectional parallel alignment with different compositions were subjected to selective isotropization by melting of the matrix HDPE material, followed by its controlled crystallization under pressure. The two processes were performed in a hydraulic press (SATIM, France) at a temperature of 160 °C and pressure of ca 8–9 MPa using heating and cooling rates of 10 °C/min. In such a way, the bundles were processed into rectangular plates (60 mm × 120 mm), 1.0–1.4 mm thick used in the next mechanical, microscopy or X-ray scattering experiments. More details about the OP and MFC preparation can be found elsewhere [32,34].

In such a way a number of MFC systems were produced (Tables 1 and 2).

2.6. Preparation of PAMC by AAP

The polymerization was carried out in a 500-mL glass flask fitted with thermometer, magnetic stirrer, Dean-Stark attachment for azeotropic distillation with reflux condenser, and inlet for dry nitrogen. In a typical synthesis, about 0.5 mol of ECL and the respective amounts of load (MMT, carbon allotrope, metal or metal oxide, etc.) were added to 100 mL of a 1:1 v/v toluene/xylene mixed solvent while stirring, under nitrogen atmosphere, refluxing the reaction mixture for 10–15 min. Subsequently, 3 mol% of DL and 1.5 mol% of C20 were added at once. The reaction time was always 1 h (from the point of catalytic system addition), keeping the temperature in the 125–135 °C range at a constant stirring of ca. 800 rpm. The loaded PAMC formed as fine powder that was separated from the reaction mixture by hot vacuum filtration, washed several times with methanol and dried for 30 min in a vacuum oven at 100 °C.

2.7. Sample characterization

The SEM studies of PAMC were performed in a NanoSEM-200 apparatus of FEI Nova (Hillsboro, USA) using mixed secondary electron/back-scattered electron in-lens detection. PAMC samples were observed after sputter-coating with Au/Pd alloy in a 208 HR equipment of Cressington Scientific Instruments (Watford, UK) with high-resolution thickness control. MFC samples were observed after cryofracture of the molded samples. Because of the low diameter of the OPs and their hardness, it turned impossible to prepare fractured samples of good quality for SEM. However, selected OP and MFC samples were observed by TEM using a Zeiss 902A microscope. The observations were done on ultrathin sections (ca. 70 nm) cut at about −130 °C with a Leica FC6 ultramicrotome equipped with diamond knife. Before the observation, the sections were stained with RuO_4.

The WAXS and SAXS patterns of OP and MFC samples were obtained at the soft condensed matter beamline (A2) of HASYLAB, Hamburg, Germany, using synchrotron radiation with λ = 0.15 nm. The sample-to-detector distance for the static WAXS measurements was set at 90 mm, the diffraction patterns being registered by means of a MAR CCD 2D detector with an exposure time of 10 s. For the SAXS measurements with melting/recrystallization the detector was repositioned at 2830 mm and a sample holder allowing for controlled heating/cooling cycles in the 30–300 °C range was used. For the SAXS experiments under strain a home-made stretching machine [35] was mounted in the beamline with the sample-do-detector distance set

Table 1
Composition of MFCs (in wt%) not containing MMT clays.

HDPE	PA6	PA12	YP
80	20	–	–
70	20	–	10
80	–	20	–
70	–	20	10

Table 2
Composition of MFCs reinforced with PA6/MMT.

MFC composition, wt%			MMT clay in PA6, wt%	
HDPE	PA6	YP	Nanomer	Cloisite 15A
80	20	–	7.5	–
77.5	20	2.5	7.5	–
80	20	–	–	5
80	20	–	5	–
77.5	20	2.5	–	5
77.5	20	2.5	5	–

at 2542 mm. The scattering patterns were recorded every 30 s with an exposure time of 23 s. Depending on the sample ductility, 13-35 SAXS data frames were collected and stored.

The synchrotron wide-angle X-ray scattering measurements with PAMC were carried out in the P03 MiNaXS mircofocus beamline at PETRA III, the German Synchrotron Source DESY in Hamburg, Germany. A Pilatus 300 two-dimensional detector (DECTRIS Ltd, Baden, Switzerland) was used, the sample-to-detector distance being 115 mm and λ = 0.969 Å. Calibration with a standard high-density polyethylene sample was performed. Linear WAXS profiles were obtained by radial integration of the WAXS images by means of the DPDAK version 0.3.2 (DESY and MPIKG, Germany) or xPolar (Precision Works, U.S.). Deconvolution of the linear profiles was made by peak fitting using a commercial software package (PeakFit version 4.12 of Systat Inc, U.S.). Separation of the total WAXS scattering into oriented and non-oriented parts was performed by the xPolar software. The SAXS two-dimensional patterns were processed and analyzed by an automatized procedure using the pv Wave® programming environment. More details about the MiNaXS beamline can be found elsewhere [36].

3. Theoretical background of the X-ray measurements

3.1. Crystallinity index determination

A semicrystalline polymeric material produces WAXS patterns representing a superposition of diffuse scattering originating from the disordered amorphous material and several sharp Bragg peaks originating from the ordered crystalline domains. A quantitative determination of the WAXS weight crystallinity w_c from isotropic WAXS patterns is possible [37,38], but rather involved. For anisotropic patterns the problem becomes even more involved because a well-founded intensity isotropization is only possible if the scattering intensity in the complete reciprocal space is known [8]. Nevertheless, if the aim is only to arrange samples in the order of increasing crystallinity, a more simple WAXS method [39] can be used to compute a crystallinity index x_c using the relationship

$$x_c = \frac{\int_0^\infty I_{cr}(s)ds}{\int_0^\infty (I(s) - I_{bg}(s))ds} \tag{1}$$

with $I(s)$ being the measured isotropic WAXS intensity, and $s = |\mathbf{s}| = (2/\lambda) \sin\theta$ representing the modulus of the scattering vector at a certain wavelength λ and scattering angle of 2θ. $I_{bg}(s)$ is the machine background as measured without sample, and $I_{cr}(s)$ is its crystalline component of the WAXS intensity above the amorphous halo. The required separation of $I_{cr}(s)$ can be performed by peak fitting programs. Since MFC materials contain several crystalline phases, their types and relative variations were studied by analyzing the number and the positions of the respective crystalline peaks contained in $I_{cr}(s)$.

3.2. Separation of X-ray scattering

If the semicrystalline polymer sample contains differently oriented and non-oriented domains, the total scattered intensity could be considered a superposition of anisotropic and isotropic scattering. They can be separated by a 2D deconvolution procedure that can be implemented to either WAXS or SAXS data [40]. Thus, the azimuthally dependent anisotropic part of

the scattering $\Phi_{aniso}(s,\chi)$ that arises from the oriented domains of the sample can be computed subtracting from the total scattering $\Phi(s,\chi)$ the azimuthally independent, isotropic scattering $\Phi_{iso}(s)$:

$$\Phi_{aniso}(s,\chi) = \Phi(s,\chi) - \Phi_{iso}(s) \tag{2}$$

where χ is the azimuthal angle. In this work the above separation of oriented and non-oriented scattering was performed with WAXS data in static experiments and with SAXS data in the simultaneous X-ray/straining experiments to quantify the evolution of nanostructure in MFC samples.

3.3. SAXS data processing

In the simplest and most frequently used analysis of SAXS data, the observed peak of the scattering curve is related to the average distance between the nanoscopic domains in the sample, called also the *long period, L.* Hence, for small scattering angles and based on the reciprocity in the Bragg law:

$$L = 1/s_{max} \tag{3}$$

with $L = l_c + l_a$. Here l_c is the average thickness of the crystalline lamellae and l_a the thickness of the interlamellar amorphous regions.

Apparently, Eq. (3) cannot be used for determination of l_c and l_a or for characterization of the size distributions of the related domains. To do that, the approach of Kortleve and Vonk [41] should be employed based on one-dimensional Fourier transform of the Lorentz corrected linear SAXS profile ($I_1(s)$), producing the linear correlation function (CF) or $\gamma_1(x)$ [8]:

$$\gamma_1(x) = \frac{2}{k}\int_0^\infty I_1(s)\cos(2\pi xs)ds = \frac{4\pi}{k}\int_0^\infty s^2 I(s)\cos(2\pi xs)ds \tag{4}$$

Analyzing the CF values for the crystallinity within the lamellar stack, values for l_c and l_a can be calculated [42,43]. Another formalism employed frequently in polymer materials is the Ruland's one-dimensional interface distribution function $g_1(x)$ (IDF) [44]. It can be computed from any one-dimensional scattering intensity $I_1(s_i)$ by Fourier transform [8]:

$$g_1(x) = -\mathfrak{F}_1\left(4\pi s_i^2 I_1(s_i) - \lim_{s\to\infty}4\pi s_i^2 I_1(s_i)\right) \tag{5}$$

By definition, IDF is proportional to the second derivative of the related CF, *i.e.*

$$g_1(x) = -k\gamma_1''(x) \tag{6}$$

For layer-stacked materials as semicrystalline polymers, IDF presents clear hints on the shape of the layer thickness distributions, the range of order, and the complexity of the stacking topology.

Both CF and IDF in their one-dimensional treatment can be used for nanostructural characterization of common isotropic polymer systems. Their application to systems that produce highly anisotropic scattering such as MFC is not straightforward. For such systems with multiphase topology and fiber symmetry other approach was developed based on the computation and analysis of the multidimensional Chord Distribution Function $z(\mathbf{r})$ or CDF [45]. For the fiber symmetrical CDF it can be written:

$$z(r_{12},r_3) = k\Delta\gamma(r_{12},r_3) = (\nabla\rho(r_{12},r_3))^{\star 2} \tag{7}$$

i.e., the CDF is the Laplacian of the Vonk's multidimensional correlation function $\gamma(r_{12},r_3)$ [46] and can be considered an extension of the Ruland's one-dimensional IDF to the multidimensional case [47].

4. Results and discussion

4.1. Transcrystallinity quantification in MFC by TEM, SEM and WAXS

Ultramicrotoming of the OP blends and MFC was extremely difficult due to their hardness and brittleness. Acceptable TEM images were produced only for four systems without MMT (Fig. 1), displaying cuts normal to the uniaxially arranged polyamide fibrils. For OP samples, almost circular cross-sections are observed with diameters in the 350–450 nm range for the PA12-containing OP (Fig. 1a and b) and up to 500 nm for the one with PA6 (Fig. 1c). The fibrils' cross-sections in the MFC with HDPE/PA6/YP = 80/20/0 (Fig. 1d) display lesser roundness but their average diameters are the same as in the respective OP.

Sample preparation for the SEM studies was possible for all MFC samples. The images obtained allowed the assessment of the microfibrils' visible average diameters (Fig. 2): 700–765 nm for the PA6-containing MFC without MMT (Fig. 2a and b), 500–600 nm for MFC with PA12 reinforcement (Fig. 2c and d) and 1.5–2.6 μm for the Nanomer containing systems with PA6 fibrils. Notably, the diameters of the fibrils in OP blends are significantly lower than the visible diameters of the fibrils after melting/recrystallization of the HDPE matrix during the MFC formation. Having in mind that the final stage of the MFC formation includes selective melting and recrystallization of HDPE matrix in the presence of crystalline and highly oriented polyamide reinforcing component [18,34], it may be therefore supposed that the microfibrils in Fig. 2 should have a polyamide
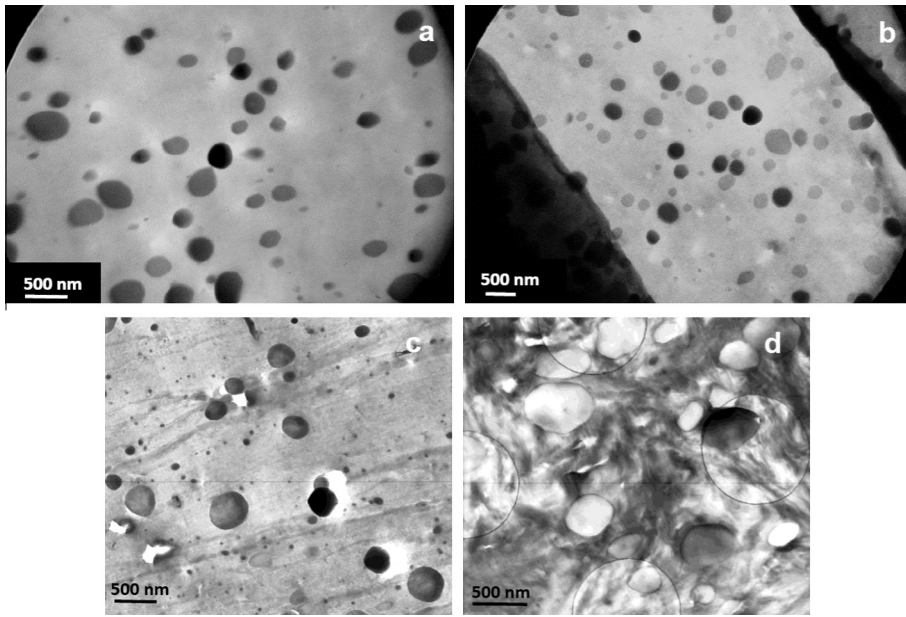
Fig. 1. TEM images of selected oriented precursors OP and MFC without MMT: (a) OP HDPE/PA12/YP = 80/20/0; (b) OP HDPE/PA12/YP = 70/20/10; (c) OP HDPE/PA6/YP = 80/20/0; and (d) MFC HDPE/PA6/YP = 80/20/0.
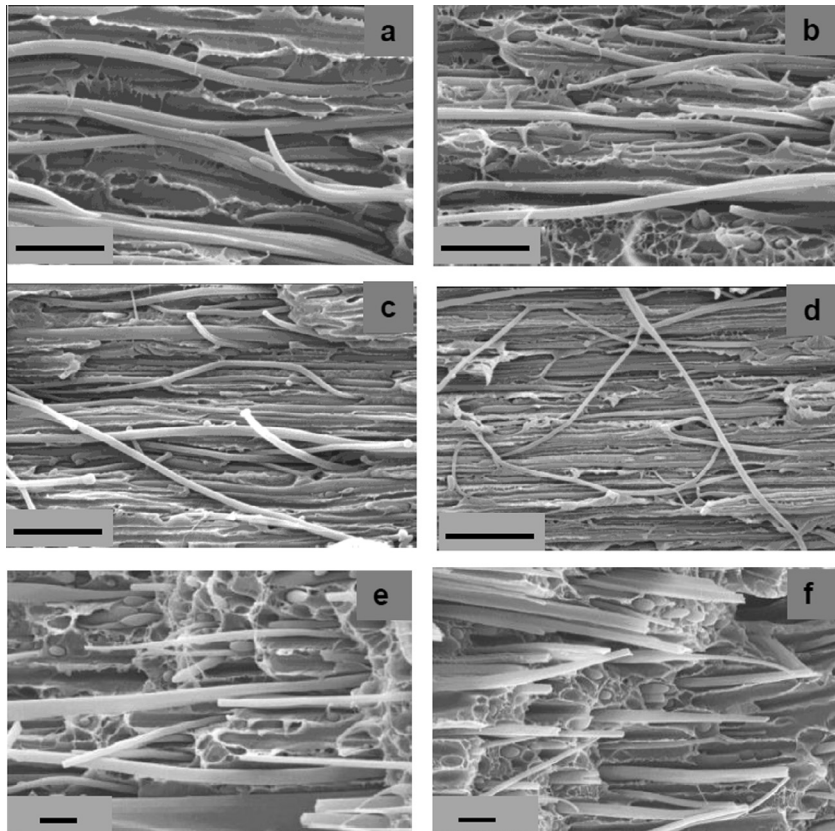

Fig. 2. Selected SEM images of MFC: (a) HDPE/PA6/YP = 80/20/0; (b) HDPE/PA6/YP = 70/20/10; (c) HDPE/PA12/YP = 80/20/0; (d) HDPE/PA12/YP = 70/20/10; (e) HDPE/PA6/YP = 80/20/0 with 5% NM; and (f) HDPE/PA6/YP = 77.5/20/2.5 with 5% NM; The scale bar in the images corresponds to 5 μm.
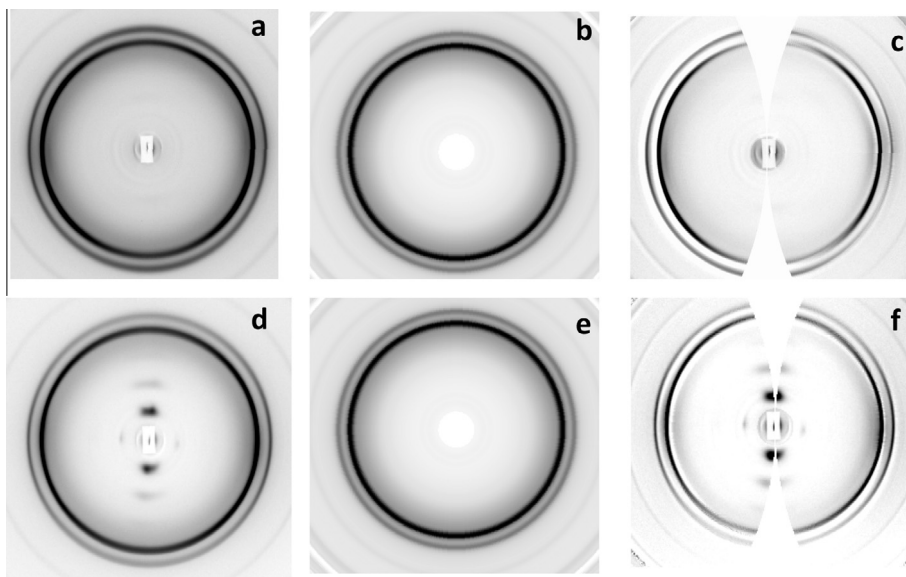
Fig. 3. Example of separation of the total WAXS ($\Phi(s,\chi)$) at 30 °C into oriented intensity $\Phi_{aniso}(s,\chi)$ and isotropic intensity $\Phi_{iso}(s)$ for two MFC samples: PA6-reinforced (a–c) and PA12-reinforced (d–f) with composition HDPE/PA/YP = 80/20/0: Left – $\Phi(s,\chi)$; Center: $\Phi_{iso}(s)$ Right: $\Phi_{aniso}(s,\chi)$ [32,34]. Fiber direction is vertical.

core covered by a transcrystalline layer of HDPE. Any other process capable to contribute to thickening of fibrils (*e.g.*, relaxation during compression molding) can be ruled out since the diameters of the PA6 fibrils observed by TEM in OP and after MFC formation by compression molding are basically the same (Fig. 1c and d).

To elucidate the morphology and microstructure of both fibrils and matrix of the MFC samples, static synchrotron WAXS patterns at 30 °C were obtained (Fig. 3). The total WAXS of a typical PA6-reinforced MFC sample (Fig. 3a) shows that the crystallographic characteristics of HDPE and PA6 are very similar with a strong overlapping of the respective reflections. The total WAXS pattern of PA12-containing MFC (Fig. 3d) reveals meridional point-like reflections of the $\gamma(020)$ crystalline planes with $d = 13{-}14$ Å. This suggests considerable orientation of the PA12 reinforcing fibrils (***b***-axis is the fiber axis) [32]. Similar $\gamma(020)$ meridional reflections with $d = 16{-}17$ Å appear in highly oriented neat PA6 but in the respective MFC they can be missing [34]. These two studies show that the PA6 microfibrils contain less γ-polymorph as they become less oriented than the PA12 microfibrils during the OP formation due to the better ductility of PA12. The total WAXS patterns of MFC with MMT based on HDPE/PA6 blends look identical to Fig. 3a.

Subtracting the non-oriented WAXS $\Phi_{iso}(s)$ that characterizes the isotropic matrix (Fig. 3b and e) from the total WAXS $\Phi(s,\chi)$ (Fig. 3a and d) for both samples in Fig. 3 reveals clearly the oriented WAXS $\Phi_{aniso}(s,\chi)$ that bears the structural information for the oriented reinforcing fibrils (Fig. 3c and f). From the last two images it can be concluded that a significant part of the HDPE matrix is able to crystallize oriented along the PA6 and PA12 fibrils thus forming an oriented transcrystalline layer in such a way that the chain directions of the two polymers coincide. The rest of the matrix HDPE situated away from the PA fibrils crystallizes isotropically.

The linear profile of the isotropic WAXS intensity $\Phi_{iso}(s)$ can readily be separated into distinct peaks in order to detect its crystallographic components. This is not the case for the anisotropic WAXS intensity $\Phi_{aniso}(s,\chi)$. Thus, for the mere purpose of component detection by peak separation from each anisotropic WAXS we computed curves according to Eq. (8):

$$\Phi_{aniso}(s) = \int_0^\pi \Phi_{aniso}(s,\chi)d\chi \tag{8}$$

that were afterwards fitted by Gaussian peaks. The reason for this simple conversion is the fact that the strict intensity isotropization cannot be performed because our oriented WAXS data are incomplete. For completion we should have measured the patterns of samples in the same state under different tilt angles and combine them into a complete view of the reciprocal space. This is extremely time-consuming considering both the measuring experiments and the mathematical treatment.

The results from peak-fitting of the $\Phi_{aniso}(s)$ for three representative MFC samples are shown in Fig. 4a–c. For the HDPE/PA6 system with 20 wt% of PA6, the oriented WAXS clearly shows the (1 1 0), (2 0 0) and (2 1 0) contributions of the HDPE and also the crystalline reflections of oriented α- and γ-PA6 polymorphs (Fig. 4a).

The same processing was performed with the oriented WAXS of a HDPE/PA12 and a HDPE/PA6-MMT composite (Fig. 4b and c). In all cases, HDPE peaks were found in the oriented WAXS, along with the typical reflections for α- and γ-polyamide phases and, in the latter case in Fig. 4c, for the MMT component. As expected, peak fitting of the
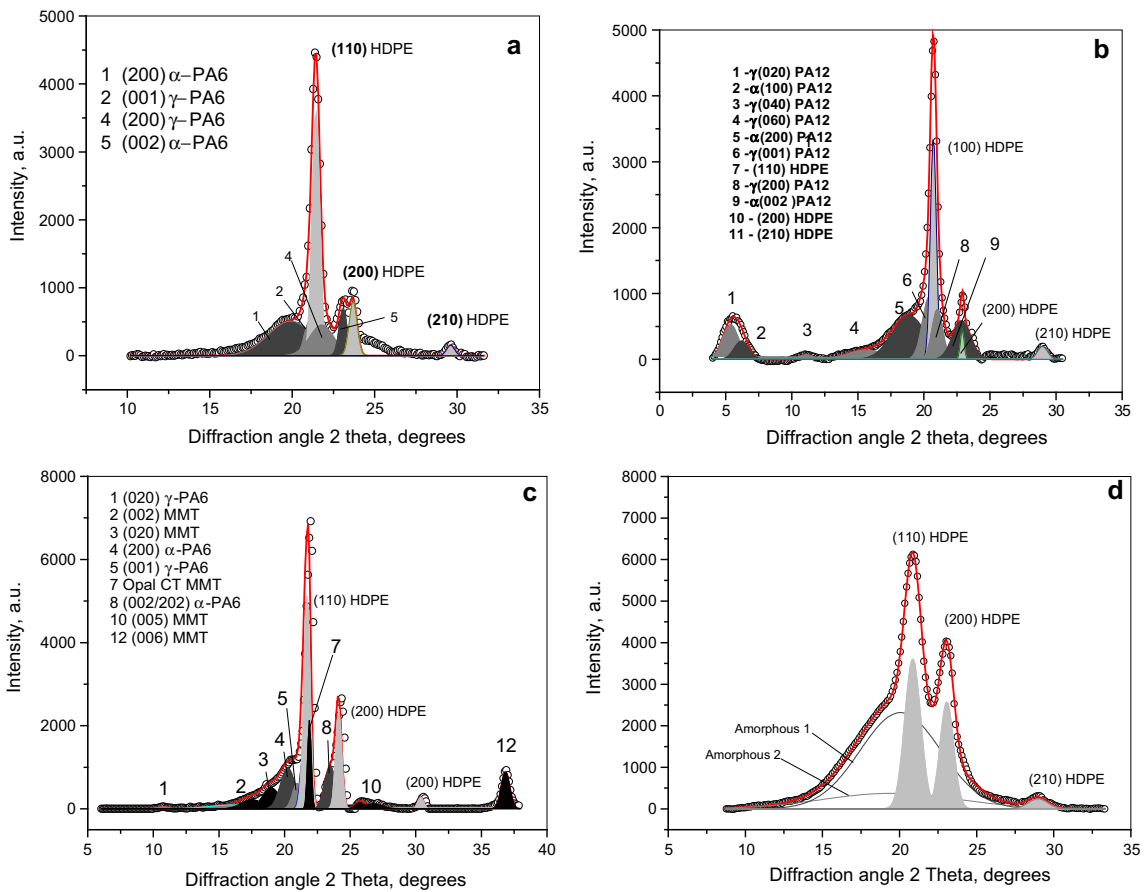
Fig. 4. Example of peak fitting for typical MFC samples after separation of the total WAXS: (a) $\Phi_{aniso}(s)$ of HDPE/PA6/YP = 80/20/0; (b) $\Phi_{aniso}(s)$ of HDPE/PA12/YP = 80/20/0; (c) $\Phi_{aniso}(s)$ of HDPE/PA6-MMT = 80/20 with 5% NM; and (d) $\Phi_{iso}(s)$ typical for the MFC samples without MMT.

Table 3
Deconvolution of the oriented and isotropic WAXS for two HDPE/PA6/YP MFC.

WAXS reflections	HDPE/PA6/YP					
	80/20/0			70/20/10		
	2θ (°)	Content (%)	d_{hkl} (Å)	2θ (°)	Content (%)	d_{hkl} (Å)
Oriented part of WAXS intensity $\Phi_{aniso}(s)$						
(2 0 0) – α PA6	19.90	28.5	4.34	19.92	28.7	4.34
(0 0 1) – γ PA6	21.05	6.6	4.11	21.35	7.6	4.07
(1 1 0) – HDPE	21.44	34.9	4.03	21.33	38.2	4.05
(2 0 0) – γ PA6	21.79	13.7	3.97	21.66	7.6	3.99
(0 0 2)/(2 0 2) – α PA6	23.09	6.9	3.75	22.99	6.9	3.76
(2 0 0) – HDPE	23.69	7.9	3.65	23.74	9.1	3.65
(2 1 0) – HDPE	29.61	1.5	2.94	29.50	1.9	2.95
PA6 fraction, %		55.7			50.8	
HDPE fraction, %		44.3			49.2	
f = PA6/HDPE		1.26			1.03	
Isotropic part of WAXS intensity $\Phi_{iso}(s)$						
(1 1 0) – HDPE	21.13	14.6	4.09	20.97	9.8	4.12
(2 0 0) – HDPE	23.56	11.4	3.67	23.48	12.6	3.69
(2 1 0) – HDPE	29.29	1.9	2.96	29.24	1.3	2.97

Note: In the isotropic part of the WAXS intensity the crystalline reflections are only presented. The difference to 100% will give the content of the amorphous HDPE and amorphous PA6. d_{hkl} is the *d*-spacing of the respective crystalline plane. The oriented reflections are considered 100% crystalline after the subtraction of Eq. (2) [34].
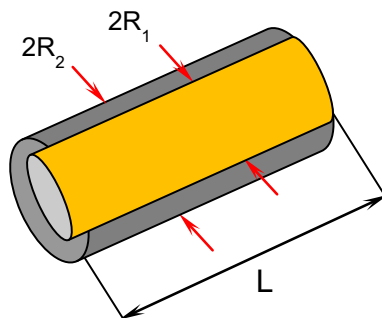
Fig. 5. Model of a shell-core polyamide fibril covered by transcrystalline HDPE.

non-oriented WAXS showed presence of crystalline HDPE only (Fig. 4d). For a good fit in this last case two diffuse peaks were necessary that should be attributed to the amorphous isotropic HDPE matrix and the amorphous fraction of the polyamide microfibrils. Notably, the oriented WAXS did not require the introduction of amorphous halo. Therefore, it may be postulated that in the HDPE/PA6 and HDPE/PA12 systems any orientation of the blend components will probably result in crystalline material.

Table 3 exemplifies the data extracted from the fitted WAXS patterns for two HDPE/PA6 MFC with and without YP compatibilizer. The percentage of WAXS produced by the oriented content of the PA6 fibrils and that of the oriented, transcrystalline HDPE is 1.03:1.00 in the compatibilized MFC and 1.26:1.00 in the non-compatibilized MFC.

This means that in the presence of compatibilizer a larger part of the HDPE is included into the transcrystalline layer without changing considerably its crystallographic characteristics. Based on the d-spacing values it can be concluded that the HDPE unit cell is slightly larger in the bulk matrix, as compared to that in the oriented transcrystalline layer (TCL).

Based on the peak-fitted oriented WAXS, results analogical to those in Table 3 can be obtained for all MFC studied. The relationship $f = \Phi_{aniso}^{PA}(s)/\Phi_{aniso}^{HDPE}(s)$ can be calculated in each case and can be further used to obtain an estimate of the TCL thickness in uniaxially oriented MFC materials. Such estimation is based on the following theoretical considerations.

In the first place, the analysis of the data in Table 3 based on the simple pseudo-isotropized contribution $\Phi_{aniso}(s)$ and its comparison to the analysis of $\Phi_{iso}(s)$ demonstrated that in the bulk isotropic fraction only HDPE is crystallized and crystallized PA6 is only found in the anisotropic fraction. Moreover, there is also anisotropically crystallized HDPE. This finding supports the morphological model sketched in Fig. 5, and a quantitative determination of the dimensions of PA core and HDPE shell is of interest.

Second, from theoretical point of view, splitting of $\Phi_{aniso}(s)$ from MFC into components from PA and PE is surely possible qualitatively. For the quantitative TCL thickness estimation one needs to separate into components the *total oriented crystalline intensity* irradiated into the complete reciprocal space. Since the information content of the measured WAXS patterns in Fig. 4 does not cover the complete reciprocal space (cf. Eq. (8)), the TCL thickness can be assessed only approximately. Two simplifying assumptions should be thereby applied: (i) the contributions of the meridional reflections of PA and HDPE can be neglected because of their weakness and (ii) mapping of the WAXS fiber data from the surface of Ewald's sphere to the (s_{12}, s_3) plane may be omitted. Then, the approximately isotropized total anisotropic component of the WAXS intensity is:

$$\tilde{I}_{tot,ani}(s) = 2\pi s \int_0^\pi \Phi_{aniso}(s, \chi) \sin\chi \, d\chi \tag{9}$$

with $\chi = 0$ defining the fiber axis and $2\pi s_{12} = 2\pi s \sin\chi$ being the circumference of the circle in reciprocal space. The corresponding total isotropic component of the WAXS is well-known, does not require approximation, and reads:

$$I_{tot,iso}(s) = 4\pi s^2 \Phi_{iso}(s) \tag{10}$$

The curves according to Eqs. (9) and (10) can be decomposed by peak-fitting, as has been done with the pseudo-isotropized curves. After identifying the broad amorphous halos and the peaks from the crystalline PA and HDPE, respectively, the total intensities $I_{tot,iso,am}(s)$, $I_{tot,iso,cr,PE}(s)$, $I_{tot,iso,cr,PA}(s)$, $\tilde{I}_{tot,ani,am,PE}(s)$, $\tilde{I}_{tot,ani,am,PA}(s)$, $\tilde{I}_{tot,ani,cr,PE}(s)$, and $\tilde{I}_{tot,ani,cr,PA}(s)$ are described by the respective peaks in Fig. 4 and numerical values in Table 3. It should be noted that the peak fitting suggests that $\tilde{I}_{tot,ani,am,PE}(s)$, $I_{tot,iso,cr,PA}(s)$ and, $\tilde{I}_{tot,ani,am,PA}$ have zero intensity.

Summarizing, in order to compute the relative thickness of the transcrystalline layer, we resort to the result of Ruland [37,38] that the scattering intensity of a certain contribution $I_c(s)$ integrated over the whole reciprocal space is proportional to the number of electrons $N_{el,c}/V$ which belong to this phase, V being the irradiated volume. This means in our notation

$$N_{el,c}/V \propto \int_0^\infty I_{tot,c}(s) ds \tag{11}$$

and the proportionality factor is a geometric factor which is the same for all components in the material. Clearly that if the WAXS intensity is an approximate one, *e.g.*, $\tilde{I}_{tot,ani,PE}$, the number of electrons will also be approximate or $\tilde{N}_{el}$. In the final computation the index c is replaced by the triple index which describes the respective component, *e.g.* $c \to ani,cr,PE$.

Table 4
Dependence between the morphological parameters of the fibrils (R_2, R_1 and TCL) calculated from WAXS or determined form SEM data and the mechanical behavior in various HDPE/PA/YP composites without MMT.

	HDPE/PA6/YP		HDPE/PA12/YP		PA6	PA12	HDPE
	80/20/0	70/20/10	80/20/0	70/20/10			
$2R_2$, nm	750	500	625	560			
$2R_1$, nm	550	350	535	453			
TCL = R_2–R_1	100	75	45	54			
E_1, MPa	1095	920	1054	972	3180	2240	827
σ_y, MPa	57	37	64	55	230	233	26
C_R, MPa	2624	2294	3414	3404	–	–	1478

Notes: E_1 is the secant modulus determined at 1% strain; σ_y, is the maximum stress at break and C_R is the three point support flexural stiffness determined according to Nunes et al. [48].

For the particular MFC samples in this study, the volume fractions of the components in the TCL are readily established after computation of the electron densities $\rho_{el,PE}$ and $\rho_{el,PA}$ of the amorphous and of the crystalline phases of PE and PA, respectively according to [8]:

$$\rho_{el,i} = N_A \frac{Z_M}{M_M} \rho_m \quad \text{[electron units/nm}^3] \tag{12}$$

with ρ_m, being the respective average mass density, N_A the Avogadro's number ($6.022 \times 10^{23} \text{mol}^{-1}$), Z_M the number of electrons per monomer unit and M_M – the molecular weight of molecule or monomer unit.

If we denote by V_{PA} the volume of the PA core, in agreement with the model in Fig. 5, it can be written that

$$V_{PA} = \pi L R_1^2 \tag{13}$$

and

$$V_{TCL} = \pi L (R_2^2 - R_1^2) \tag{14}$$

Combining Eq. (10) with 11 and 12, the following simple dependence can be deduced between the visible by SEM fibril radius R_2 and that of the PA core R_1:

$$R_1^2 = R_2^2 \cdot \sqrt{\frac{f}{k+f}}, \tag{15}$$

wherein $k = \rho_{PA}/\rho_{HDPE}$ and $f = \Phi_{aniso}^{PA}(s)/\Phi_{aniso}^{HDPE}(s)$.

Table 4 summarizes the structural information related to the reinforcing fibrils as revealed by SEM and WAXS methods (*i.e.*, $2R_1$, $2R_2$ and $R_2 - R_1$) for MFC materials without MMT reinforced by either PA6 or PA12. The $2R_2$ values were obtained by averaging of 3–5 fibril thicknesses per sample as measured during the SEM observation. The same table contains also the respective data for the Young's modulus E_1, stress at break σ_y, and flexural stiffness C_R, of the respective MFC as well as of the neat HDPE matrix and the neat oriented polyamides.

It can be concluded that the formation of transcrystalline layers TCL is a common feature for all MFCs containing either PA6 or PA12. There can be a significant difference between the TCL thicknesses in PA6 and PA12 reinforced composites, as well as in the compatibilized and non-compatibilized MFCs with the same reinforcement. Compatibilization results in thinner fibrils in which not only the polyamide core, but also the TCL are finer. In the PA6 reinforced MFC the TCL is notably thicker than in the PA12-containing system. Judging from Table 4, the TCL thickness can be related to the mechanical performance of the MFCs. No matter that the E_1 value of neat oriented PA6 is much higher than that of oriented PA12, the respective compatibilized and non-compatibilized MFC display similar moduli. At the same time, the σ_y of the HDPE/PA12/YP materials are significantly higher, irrespective of the almost coinciding values of the neat oriented polyamides. It is to be noted the superior flexural stiffness of the PA12-reinforced MFC. This can be attributed to the lesser TCL thickness and the better orientation of the PA12 fibrils achieved in the stage of cold drawing.

Table 5 presents the information extracted from SEM and WAXS measurements of HDPE/PA6 MFC with and without YP compatibilization, in which the fibrils are loaded with different amounts and types of MMT nanoclays. Again, data for E_1, σ_y, and C_R are presented to allow a comparative analysis.

It can be seen that the compatibilizer, the clay amount and type affect significantly the TCL thickness. Thus, 5% of NM and CL15A produce similar thicknesses in non-compatibilized MFC and quite identical E_1 and C_R values, σ_y being slightly higher in the latter case. Clay load of 7.5% NM is related to a notable TCL increase resulting to superior modulus and flexural properties but a drop in the tensile strength. This MFC displayed the thickest PA6 fibrils obviously due to a lower orientation in the cold drawing stage of preparation. Introducing 2.5% of YP compatibilizer results in finer fibrils *i.e.*, lower $2R_2$ values and finer TCL, not so strongly depending on the clay amount and type. In the NM-containing compatibilized MFC the σ_y values increase, the difference in E_1 and C_R depending on the amount than on the type of the clay.

Table 5
Dependence between the morphological parameters of the fibrils (R_2, R_1 and TCL) calculated from WAXS or determined from SEM data and the mechanical behavior in various HDPE/PA6/YP composites containing various amounts and types of MMT nanoclays.

	80/20/0 + MMT			77.5/20/2.5 + MMT		
	NM 5%	NM 7.5%	CL15A 5%	NM 5%	NM 7.5%	CL15A 5%
$2R_2$, nm	1250	1750	1320	1050	1100	1200
$2R_1$, nm	1104	1508	1176	923	984	1100
TCL = $R_2 - R_1$	73	121	72	64	58	50
E_1, MPa	1191	1244	1161	1215	1288	1187
σ_y, MPa	45	39	53	59	56	55
C_R, MPa	2500	2850	2420	2590	2950	2340

Comparing the data in Tables 4 and 5, it can be concluded that the thickness of TCL in the non-compatibilized MFC in this study seems to be inversely proportional to the tensile strength. Moreover, in MFCs without MMT a thinner TCL will result in higher E_1 and C_R values since its dampening effect will be lower. In the MMT-containing MFC this effect is inversed most probably due to migration of MMT from the PA6 fibril to the TCL. Compatibilization with YP, in general, results in thinner TCL whereby in the samples without MMT (Table 4) all mechanical properties drop which is not the case in the dually rein-forced MFC in Table 5. This can be explained with the fact that in non-compatibilized MFC the formation of TCL would involve HDPE matrix material only. In the compatibilized ones, however, there is a chemical reaction between the maleic anhydride of YP and the amide groups of the polyamide [49]. It can be expected that here the TCL will include polyolefin component from the YP compatibilizer, which is different from the bulk matrix HDPE, which could explain the mechanical properties of the compatibilized MFC.

As noted above, the TEM image of the MFC (Fig. 1d) does not provide visualization of the TCL. Microscopy observation of TCL in MFC based on HDPE/PA blends has not been successful so far. To the best of our knowledge, TCL was directly observed in two MFC systems. Friedrich et al. [50] reported a TEM image of MFC based on poly(ethylene terephthalate (PET)/low-density PE showing the cross-section of a PET fibril covered by TCL of LDPE with a thickness of ca. 140 nm, *i.e.* close to some of the values in Tables 5 and 6. More recently, Lin et al. [51] studied by AFM a polypropylene (PP)/PET MFC proving a TCL of oriented PP of ca. 200 nm. This lack of microscopy evidence of TCL in MFC justifies the search of alternative methods of its quantification by X-ray techniques.

4.2. Microstructure evolution in MFC by simultaneous SAXS/straining experiment

4.2.1. SAXS patterns processing

Fig. 6 displays a scheme of the various stages of SAXS pattern processing. Fig. 6I shows the total scattering intensity $\Phi(s, \chi)$ of a pre-processed SAXS frame of a MFC that, according to Eq. (2), represents a superposition of anisotropic and isotropic SAXS. Fig. 6II displays the anisotropic SAXS $\Phi_{aniso}(s, \chi)$ presenting a pattern with axial symmetry with two reflections along the vertical axis of orientation s_3. This distinction was impossible in the starting Fig. 6I due to the masking effect of the iso-tropic scattering $\Phi_{iso}(s)$ (Fig. 6, III) as it was in the initial WAXS patterns in Fig. 3.

As shown further in the text, analyzing $\Phi_{aniso}(s, \chi)$ and $\Phi_{iso}(s)$ of SAXS separately would be advantageous for a better nanostructural characterization of the respective morphological entities – the TCL-covered polyamide fibrils and the isotro-pic HDPE matrix that form MFC. Assuming a multiphase topology, its nanostructure related to $\Phi(s, \chi)$ can be visualized in real space using the multidimensional CDF $z(r_{12}, r_3)$ by its respective negative and positive faces, or in absolute values (Fig. 1, IV).

It should be noted that the CDF in Fig. 6, IV consists of narrow negative and positive peaks, directly reflecting probability distributions. The negative part of CDF (*i.e.,* −CDF) contains information on the arrangements of the crystalline domains (lat-tice properties). The positive face of CDF gives a presentation of the domains themselves in the real space [45]. For the sam-ples in this study the first long-period peak of −CDF was selected. Fitting the cap of this peak to bivariate polynomials returns information about its position (L) and lateral breadth (σ_{12}). The meaning of L is the most probable long period in axial direction.

The parameter $e_l = 3\sigma_{12}$ is a measure of the extension of the crystalline domains in lateral or in r_{12} direction. Therefore, supposing that $L(t)$ is the long period at time t, and $L(0)$ is the long period at the beginning of a deformation experiment, then the nanoscopic axial elongation can be determined as:

$$\varepsilon_n(t) = \frac{L(t) - L(0)}{L(0)} \tag{16}$$

Similarly, the nanoscopic lateral elongation can be defined as [9]

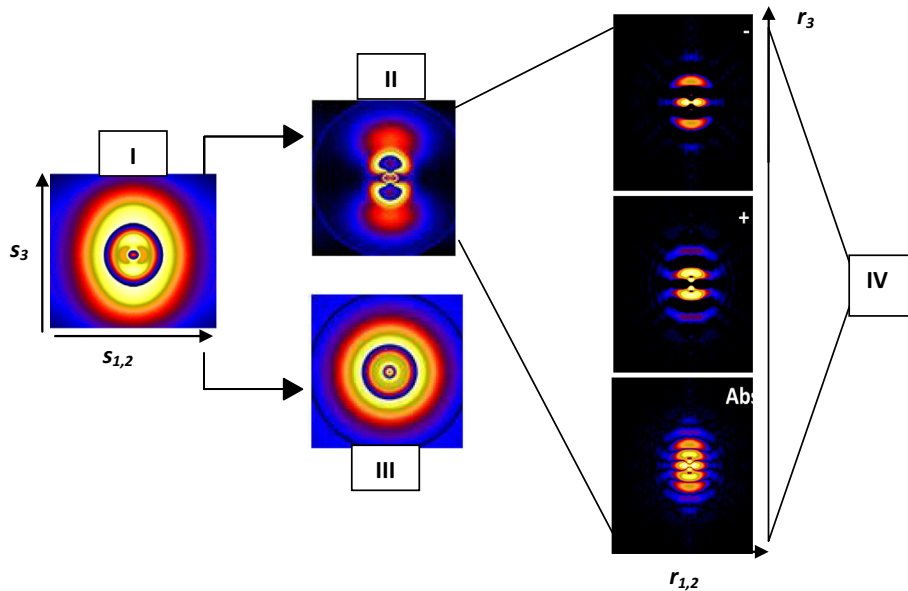$$\varepsilon_{n,r12}(t) = \frac{e_l(t) - e_l(0)}{e_l(0)} \tag{17}$$

Fig. 6. Stages of processing of the SAXS patterns: (I) reconstructed, calibrated and background corrected total SAXS data frame $\Phi(s,\chi)$; (II) azimuthally dependent scattering $\Phi_{aniso}(s,\chi)$; (III) azimuthally independent scattering $\Phi_{iso}(s)$; and (IV) various representations of the anisotropic CDF $z(r_{12},r_3)$: (−) the negative face; (+) the positive face and (abs) both faces presented as $|z(r_{12},r_3)|$. The s_3- and r_3-axes match the stretching direction of the sample.

4.2.2. Characterization of TCL in MFC without MMT during continuous strain

Most of the –CDFs obtained prior to straining do not allow identification of peaks at small r-values related to the PA6 fibrils. As the strain grows, such peaks appear but their attribution to PA6 without any proof appears doubtful. Studying the high temperature –CDFs of oriented precursors OP and the respective MFC without MMT resolves this issue (Fig. 7).

The –CDF images of the OPs with and without YP compatibilizer, at 30 °C (Fig. 7, column 1) suggest highly oriented nanostructure from slender domains with one-dimensional arrangement in rows along the vertical fiber axis. The non-compatibilized sample 80/20/0 shows four long period peaks corresponding to five correlated HDPE lamellae. In the 70/20/10 precursor the 3rd and 4th long period peaks become diffuse and merge meaning that compatibilization introduces disorder in the HDPE component. The long periods L measured from the first minimum of the –CDFs for the two OP samples at 30 °C vary in the 18–19 nm range.

The second column of Fig. 7 displays the –CDF peaks of the OP samples heated at 160 °C. As expected, the HDPE peaks disappear since all oriented polyethylene melts and its SAXS transits from $\Phi_{aniso}(s,\chi)$ to $\Phi_{iso}(s)$. Therefore, $\Phi_{aniso}(s,\chi)$ and the respective $z(r_{12},r_3)$ at 160 °C will provide information about the nanostructure of the neat PA6 microfibrils. The registered long spacings of ca. 7 nm are typical of oriented PA6 [52]. A second diffuse long period peak was observed indicating correlation of three PA6 domains along the fiber axis in all OP samples.

The third column in Fig. 7 displays the –CDF peaks of MFC materials at 30 °C. Their preparation by compression molding of the respective OP at 160 °C under pressure followed by gradual cooling creates conditions for deposition of TCL of oriented HDPE onto the polyamide fibril. The long period peaks of MFC prior to heating of $L = 23$–24 nm are related exactly to those transcrystalline polyethylene domains. They show a microfibrillar system with 1st and 2nd order long periods *i.e.*, axial correlation of three transcrystalline HDPE domains.

Column 4 in Fig. 7 shows the nanostructure of the PA6 reinforcing fibrils in the MFC revealed by selective melting at 160 °C. First-order long periods in the range of 7–8 nm with clear indication of 2nd and higher order peaks are observed, especially in the 80/20/0 MFC. This is evidence for better correlation in straining direction of crystalline PA6 domains in this sample. Notably, in the MFC with 10% YP the peaks show some curvature indicating less perfect orientation of the fibrils, just like in the OP with the same composition. Comparing the –CDFs at 160 °C of the MFC (column 4) and the respective OP (column 2) allows the conclusion that the moderate pressure and temperature applied during the MFC preparation acted toward increasing the order in the PA6 oriented domains.

Fig. 8 displays the evolution of the –CDF of two MFC without (*a*) and with 10 wt% of YP compatibilizer (*b*) at three different stages of the SAXS/straining experiment: prior to any deformation ($\varepsilon_m = 0$), and after given time of continuous deformation *i.e.*, in the middle of the straining ($\varepsilon_m = 7$–10%) and just before sample failure but still under strain at $\varepsilon_m = 15\%$ or 36% for the MFC without and with YP, respectively.

The analysis of the real-space images of the two MFCs in Fig. 8 shows that in the central areas of both starting –CDF images without strain no peaks for PA6 are observed at low r values. As the macroscopic strain grows, first, an equatorial peak with L in the range of 16–17 nm appears (marked with arrow in Fig. 8a) and at the same time the first long period peak
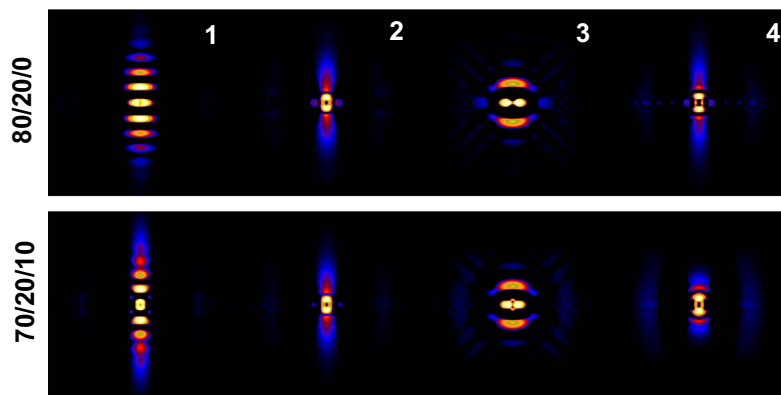
Fig. 7. Comparison between the negative faces of CDF $z(r_{12}, r_3)$ for oriented precursor blends (OP) and microfibrillar composites (MFC) with various compositions (Table 1). 1 – OPs at 30 °C; 2 – OPs at 160 °C; 3 – MFCs at 30 °C; 4 – MFCs at 160 °C. Displayed regions: −100 nm < r_{12}, r_3 < 100 nm. In all patterns fiber axis and strain direction are vertical and coincide with the r_3-axis.
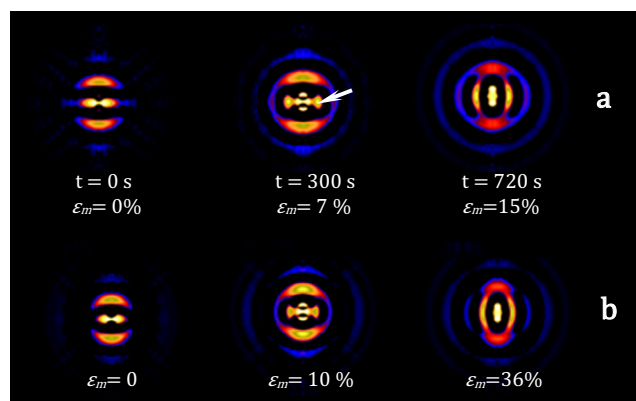

Fig. 8. Evolution of the nanostructure of the oriented –CDF $z(r_{12}, r_3)$ in MFC without MMT. Compositions, HDPE/PA/YP (wt%): (a) 80/20/0 and (b) 70/20/10. Displayed regions: −100 nm < r_{12}, r_3 < 100 nm. In all patterns fiber axis and strain direction are vertical and coincide with the r_3 axis. The arrow points at the equatorial reflection appearing under strain.

of PA6 becomes visible on the meridian with L values of 6–7 nm. The shape, orientation and number of the negative faces of the CDFs of the two MFC in Fig. 8 before straining show meridional correlation of three transcrystalline HDPE domains arranged on the top of one another. As the strain increases, these peaks become narrower meaning that the variation of the distances between the crystalline domains decreases. The strong point-like equatorial reflections that appear in the –CDFs of both MFC samples at low strain are due to lateral correlations among *HDPE domains in TCL* covering the reinforcing fibril and such belonging to matrix material in close vicinity. The second HDPE domain necessary for this correlation to appear is most probably formed by strain-induced crystallization. A similar phenomenon was observed recently in the HDPE/PA6 and HDPE/PA12 oriented precursor blends, subjected to load-cycling [53]. The weaker ark- and circular reflections in –CDF in Fig. 8 appearing under strain are most probably related to strain-induced crystallization *in the volume of the HDPE matrix*, away from the reinforcing fibril.

Fig. 9 presents a quantification of the tensile properties and nanostructural changes in the samples with compositions HDPE/PA6/YP = 80/20/0 and 70/20/10 as a function of the true stress σ and the true elongation ε_m. In both graphs the abscissa indicates the time from the beginning of the straining, and the ordinate – the evolution of six parameters (two mechanical and four structural) during the experiment, each of them being in its respective dimension. The structural parameters are: the long period values related to the peaks of transcrystalline HDPE (meridional L_m^{HDPE} and equatorial – L_{eq}^{HDPE}), to the PA6 reinforcing fibrils (meridional L_m^{PA6}), and the lateral extension e_l of the HDPE domains from TCL. These parameters were computed from the respective –CDFs during the straining experiment applying an automatic procedure [9].

The stress at break σ_b and the macroscopic strain at break ε_{mb} of the two samples show that the non-compatibilized MFC (Fig. 9a) is less ductile than the one with 10% YP (Fig. 9b), showing ε_{mb} values of 15% and 36%. At the same time, the σ_b values of 50 MPa in the non-compatibilized sample is significantly higher than that of the YP-containing sample being slightly above 30 MPa. These stresses and strains at break are in good agreement with previously published mechanical data of MFCs [34,54].

Despite their different mechanical behavior, the two MFC in Fig. 9 display similar structural developments under continuous strain. The starting L_m^{HDPE} values in both MFCs are in the range of 22–23 nm and gradually grow to 32 nm just before sample failure. Notably, there is no such growth in the long periods related to the isotropic matrix HDPE (L_{iso}, shown only in Fig. 9a). The starting L_{iso} values in both composites are identical to L_m^{HDPE} and at the end of the straining experiment even drop with 1–2 nm. The long periods of the reinforcing fibrils L_m^{PA6} vary very slightly between 6 and 7 nm, being independent of the compatibilizer content. The equatorial long spacing L_{eq}^{HDPE} in the two MFCs related to the strain-induced crystallization of HDPE domains from the matrix, appears abruptly at about 7–8% of strain with values of 16–17 nm, increasing to 19–20 nm close to sample failure. The presence of compatibilizer YP causes some structural differences. In the non-compatibilized 80/20/0 MFC the lateral extension e_l of the HDPE domains from TCL before strain is 33 nm, passes through a maximum of 41.5 nm at ε_m close to 10% and then decreases reaching just before break its initial values. Instead, in the 70/20/10 MFC e_l monotonously grows from 35 to 45 nm.

The $|z(r_{12},r_3)|$ images in Fig. 10 show the both CDF faces of two MFC sample before and after mechanical failure. Interestingly, the equatorial long spacing for the second HDPE domain in TCL with L between 17 and 30 nm disappears (cf. the images in columns 1 and 2). Hence, the suggested strain induced crystallization is a reversible process for the MFC materials without MMT.
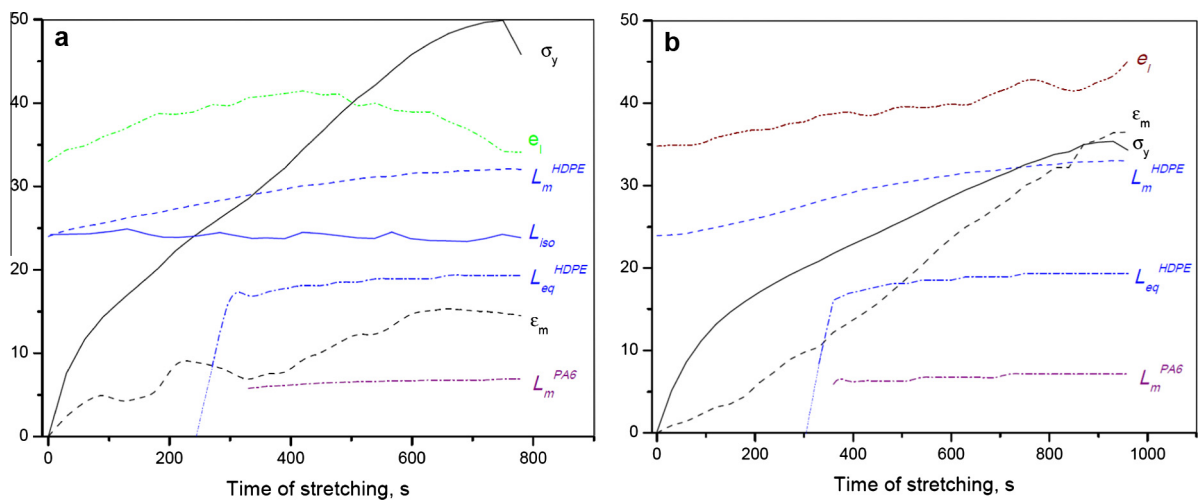

Fig. 9. Evolution of the nanostructural and mechanical parameters during the simultaneous SAXS/straining of MFCs without additional clay reinforcement: (a) HDPE/PA6/YP = 80/20/0; (b) HDPE/PA6/YP = 70/20/10. All nanostructural data are obtained from the respective -CDF peaks computed on the basis of azimuthally dependent $\Phi_{aniso}(s,\chi)$. Legend: stress σ [MPa]; macroscopic strain ε_m [%]; meridional long period of transcrystalline HDPE domains L_m^{HDPE} [nm]; equatorial long period L_{eq}^{HDPE} [nm] of strain-crystallized HDPE; meridional long period L_m^{PA6} [nm] of PA6; lateral extension e_l [nm] of the meridional transcrystalline HDPE domains.
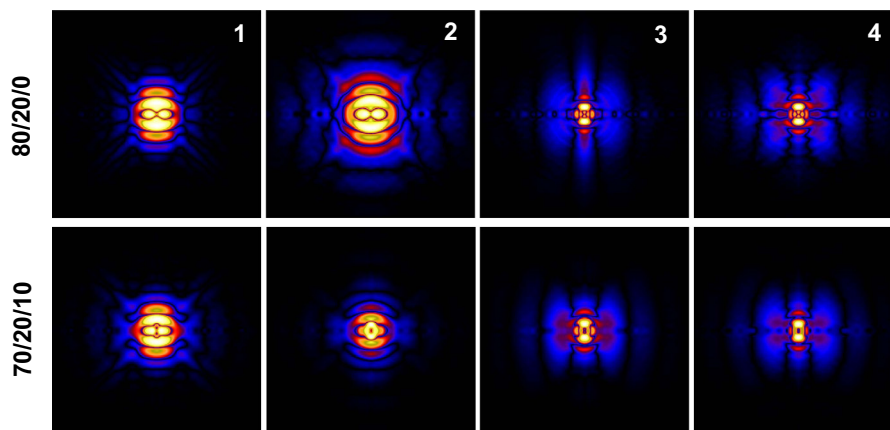

Fig. 10. Comparison between the $|z(r_{12},r_3)|$ for MFCs without and with compatibilization before strain and after sample failure and relaxation: 1 – MFCs before strain at 30 °C; 2 – MFCs after mechanical failure at 30 °C; 3 – MFCs before strain at 160 °C; 4 – MFCs after strain and relaxation at 160 °C. Fiber axis and strain direction are vertical.

Moreover, analyzing the CDF shapes and positions, an axial growth of the transcrystalline HDPE domains from 23–24 to 27 nm is observed due to the extreme mechanical load. In the uncompatibilized 80/20/0 MFC the perfection of the transcrystalline HDPE domain orientation is decreased, which is evidenced by the change of shape of the CDF peaks. In this sample the loss of correlation among the domains in straining direction is low. In the HDPE nanostructure of the compatibilized 70/20/10 MFC the extreme mechanical load causes mainly a relative decrease of the lateral extension of the domains, *i.e.*, a transition from lamella to grain.

The changes in the PA6-nanostructure can be studied from the CDF patterns at 160 °C (Fig. 10, columns 3 and 4). The uncompatibilized MFC before straining shows highly ordered PA6 microfibrils almost uncorrelated in lateral direction, which after sample failure gained such correlation. The off-meridional streaks have moved closer to the meridian, there is even a 2nd order of off-meridional streaks. This indicates the beginning of 3D macrolattice formation. In the compatibilized material such macrolattice inside the PA6 microfibrils exists even before straining and the ultimate loading results in a slight decrease of its correlation.

Combining the information from Figs. 8–10, a model of the scattering ensembles existing in the MFC at various stages of the straining can be suggested. The cartoon in Fig. 10 visualizes the reversible strain-induced crystallization of matrix material in the presence of the oriented transcrystalline HDPE shell of the PA6 reinforcing fibrils.

Fig. 11a depicts the three transcrystalline HDPE domains on the PA6 fibril surface correlated along the sample meridian. Before straining, the lamellae tip domain is in contact with amorphous HDPE matrix material containing macromolecules with varying degree of entanglements. At low strains ($\varepsilon_m < 7$–10%) the tip TCL domain grows in lateral direction involving some less entangled HDPE macromolecules that are able to crystallize (Fig. 11b, the arrow-indicated process). As seen from Fig. 9, the lateral lamellae extension e_l in the YP-containing MFC is constant with the strain increase until sample failure, while in MFC without compatibilization it passes through a maximum. In agreement with the "minimum crystallization distance" concept of Strobl, the highly entangled zone cannot be entered by any other crystalline lamella growing during the strain-induced crystallization [55]. Therefore, the process is transferred to the next crystallizable area. Above a certain density of the stress field (at $\varepsilon_m > 7\%$ for the 80/20/0 sample and above 10% for the 70/20/10 one), a new (called also "satellite") HDPE crystalline domain appears (Fig. 11c, *ii*), its far end being quite well defined with respect to the tip domain. Judging from the CDFs in Fig. 8, it seems that for both MFCs in the beginning of the straining the tip and the satellite domains are positioned in front of each other, *i.e.,* normally to the straining direction. As the strain increases, this perfect frontal alignment becomes distorted and the satellite domain may be repositioned slightly above or below the tip domain as depicted by the dashed lines in Fig. 11c. After sample failure (Fig. 11d), the satellite domains melt and the axial correlation of three HDPE domains is preserved in both MFC. In the non-compatibilized MFC some loss of their axial alignment (*i.e.*, different inclinations in respect to the normal to the straining direction) may be deduced. In the compatibilized MFC, where the TCL domains are chemically bonded to the PA6 fibril (the dot in Fig. 11c), their lamellar geometry transits into grains as schematically indicated in the same figure.

4.2.3. Characterization of TCL in MFC with MMT

The MFC containing MMT nanoclays located predominantly in the PA6 oriented fibrils were also studied in SAXS/straining experiments as well as at different temperatures before and after strain. This section summarizes the results obtained comparing them to the analogues without clay.

The structures of the HDPE from TCL in MFC at 30 °C without and with MMT (Fig. 12, images a and c, respectively) as presented by the respective $|z(r_{12}, r_3)|$ functions seem to be quite similar. Eliminating the HDPE reflections from TCL by heating at 160 °C (Fig. 12b and d) and comparing the resulting CDF at this temperature, it appears that the PA6 microfibrils containing MMT are built of longer and straighter crystalline domains. This makes the inter-fibrillar distance shorter than in the respective MFC without MMT. Such an effect seems to be natural: a bunch of the wavy microfibrils of the MFC without MMT must maintain a wider distance from each other compared to a bunch of straight fibrils. Moreover, in the sample with MMT the off-meridional peaks indicate some lateral correlation among the PA6 crystallites suggesting arrangement in a
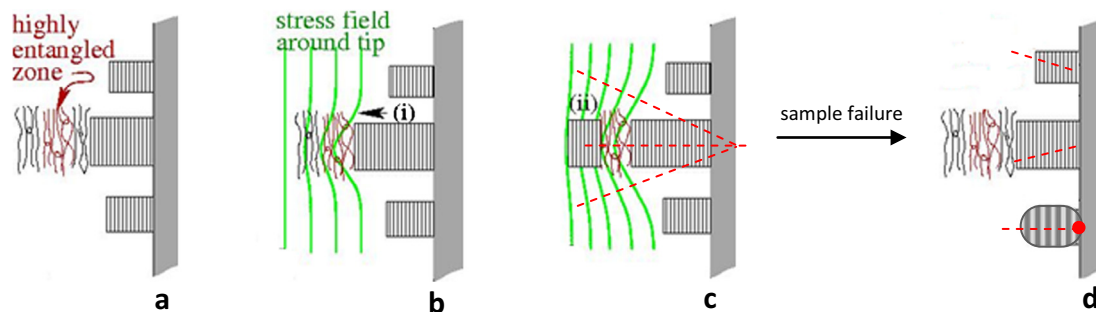

Fig. 11. Schematic presentation of the strain-induced crystallization of HDPE matrix material during the continuous strain of HPDE/PA6 microfibrillar composite: (a) at $\varepsilon_m = 0$; (b) at $\varepsilon_m < 7$–10%; (c) at $\varepsilon_m > 7$–10%; (d) after sample failure. *i* – tip HDPE domain and the direction of its growth; *ii* – strain-crystallized (satellite) HDPE domain. For more details see the text.
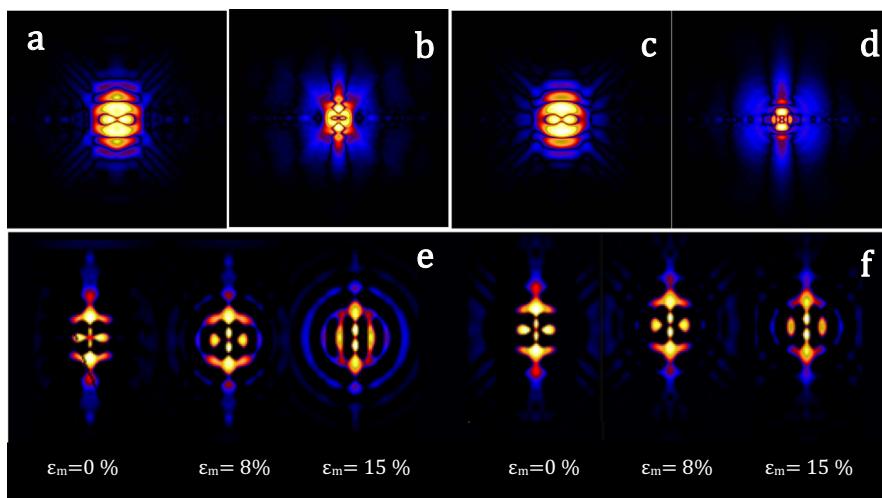
Fig. 12. CDF images $|z(r_{12}, r_3)|$ of various MFC with composition HDPE/PA6/YP = 80/20/0: (a) with 5% NM, at 30 °C; (b) same as a, at 160 °C; (c) no MMT, at 30 °C; (d) no MMT, at 160 °C; (e) with 5% NM strained at 30 °C; (f) with 5% CL15A strained at 30 °C; Images a trough *d* present both negative and positive faces of CDF; images e and f present the −CDF faces. Fiber axis and strain direction are vertical.

rudimental 3D lattice. Notably, the PA6 domains in MFC with MMT vary in the range of 9–10 nm, which is above the values of 6–7 nm in the HDPE/PA6/YP composites without MMT (Figs. 8 and 9).

Fig. 12 displays also the −CDF faces computed from the oriented SAXS in two MFC samples containing 5% of NM or CL15A in a straining experiment. Three different stages of the straining process are considered: before deformation ($\varepsilon_m = 0$), toward the middle of the straining ($\varepsilon_m = 8$–9%),) and at a certain point before the sample failure at $\varepsilon_m = 13$–15%. Analyzing the images of the MFC with NM (Fig. 12e) or CL15A (Fig. 12f), in equatorial direction one observes even at $\varepsilon_m = 0$ peaks with $L = 12$–14 nm growing up to ca. 20 nm as the strain increases. As with the samples without nanoclay, these peaks can be attributed to lateral correlation of HDPE tip and satellite domains (Fig. 11). In the present case, however, these satellite domains are not a result of strain-induced crystallization but they are present before application of strain. At $\varepsilon_m = 0$, as in the samples without MMT, the positioning of the satellite and tip domain is frontal since the equatorial reflections are almost point-like. At $\varepsilon_m = 14$–15% this arrangement is distorted (better expressed in the NM-containing MFC) reflected by the formation of arcs. In axial direction the two samples with 5% MMT display correlation of at least three narrow HDPE domains. Interestingly, the PA6 peaks are also clearly observable in the negative faces even at 30 °C in both samples in Fig. 12e and f as two bright points on the meridian, right in the center of the images. The respective PA6 long spacings remain constant during the strain, right until the sample failure. Summarizing, the presence of MMT induces irreversible crystallization in the vicinity of the TCL/-fibril ensemble even without strain, maintaining the nanostructure of the ensemble quite constant until sample failure.

4.3. Microgradients in differently loaded PAMC by microfocus synchrotron WAXS

It has been repeatedly recognized that natural and synthetic anisotropic materials whose composition changes gradually (*i.e.,* without interfaces or layers) along a certain axis can possess unique mechanical, optic and other properties [56]. Therefore, the rigorous evaluation of gradients at micro- and possibly at nanoscale in various materials seems to be interesting from both theoretical and practical aspects. This section demonstrates the possibility to study concentration microgradients in PAMC loaded with various inorganic materials by means of microfocus synchrotron WAXS.

As seen from Fig. 13, PAMC loaded with MMT are porous objects with diameters typically in the 20–50 μm range. Conventional SEM reveals the topology of PAMC but not the distribution of the MMT (Fig. 13a and b).

The clay nanoparticles with sizes in the 80–110 nm range can only be visualized in mixed SEM/TEM mode after mechanical crushing of PAMC in liquid nitrogen (Fig. 13c). It should be noted that this method results in good visualization very rarely, not providing any information about the gradients in the fine structure of either MMT load or polyamide shell, *e.g.,* degree of exfoliation in various points of the microcapsule, polymorph content, degree of crystallinity, *etc.* In an attempt to study the variation of these structural features at microscale, differently loaded PAMC were scanned with a 5 × 5 μm microfocused beam.

Fig. 14 displays a typical PAMC sample visualized in a Keyence model VHX-600 digital light microscope. The microcapsules are placed as a monolayer on a polymeric sticky tape not producing own crystalline peaks in WAXS. The area of the sample to be scanned by the microbeam and the size of the latter are visualized in the same figure.

The sticky tape with the PAMC was placed in sample holder mounted vertically on a motor-powered XZ sliding stage positioning the beam in point X1,Z1 of the grid (Fig. 15a, the solid square).
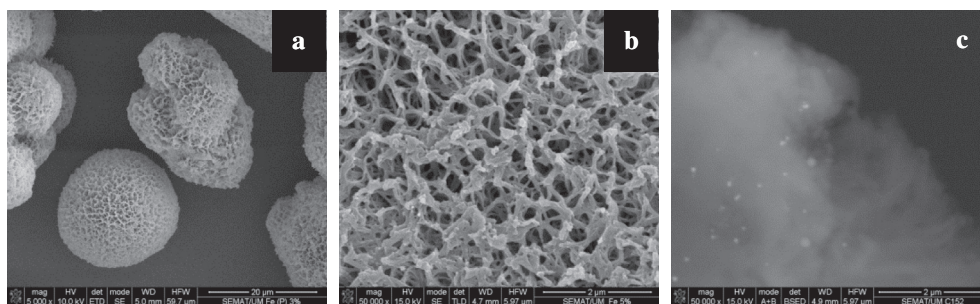
Fig. 13. Morphology of MMT-loaded PAMC: (a and b) SEM images with coating; (c) image obtained in mixed SEM/TEM mode without coating after cryogenic milling.

Fig. 14. Light microscopy image of PAMC before their insertion into the microfocus WAXS beamline. The small solid square depicts the size of the WAXS microfocus related to the sample area scanned (the big square) and the size of the loaded PAMC.

The beam was switched on and the sliding table started moving along the Z1, X1-11 direction (the white arrow in Fig. 15a) making 11 steps of 5 μm (*i.e.*, the microbeam size), the irradiation time in each point being 5 s. Then, the beam goes to grid square Z2,X1 and makes another scan in horizontal direction. The procedure is repeated until covering the whole sample grid. All 2D patterns obtained (looking very similar to that in Fig. 3a) were stored and integrated radially in the 0–360° area to obtain the respective 121 linear profiles.

Fig. 15b shows the 11 WAXS patterns taken at level Z3 (X index increasing from bottom to top). It can be seen that the 001 basal MMT peak in the 2–4° 2θ range indicating correlation of silicate platelets and hence lack of exfoliation appears only in positions X1–X3 after which it disappears, *i.e.*, in the rest of the grid cells along the Z3 line the sample is fully exfoliated. At the same time, the 14–16° 2θ region of the WAXS patterns displays the intensity of the crystalline peaks of the PA6 and will thus quantify the distribution of the matrix material within the area scanned. Fig. 15c and d shows the full 11 × 11 intensity maps for a PAMC sample with 2% NM in the low and medium 2θ range, respectively. It can be seen that Fig. 14d visualizes quite clearly the silhouettes of the polyamide microcapsules in the scanned sample area with sizes in the range of 20–30 μm while Fig. 15c represents the distribution of domains with exfoliated (blue–gray)[1] and non-exfoliated MMT (green–yellow) within the same sample area.

The same analytical method was used to study the microgradients in PAMC loaded with CL15A, GR, Al and Fe_3O_4. The intensity maps characterizing the load distribution (left column) and the PA6 distribution (right column) within the scanned area are presented in Fig. 16.

Various observations can be made comparing the load- and PA6-shell distribution maps in Figs. 15 and 16. Thus, from Fig. 15a (NM-loaded PAMC) and Fig. 16a (PAMC/CL15A) it seems that latter sample displays smaller and more homogeneously distributed domains of non-exfoliated MMT, in which the basal peak is of lower intensity at similar particle packing on the scanned area. In these two samples the domains with non-exfoliated MMT are definitely smaller than the PAMC sizes. In the case of GR and especially with Al load (Fig. 16c–f), the shape and size of the domains taken by the load and by the PA6 shell almost coincide, which is an indication that in these PAMC in fact enclose a few or even one single load particle. This is in good agreement with the particle sizes of GR and Al of several microns as established in previous SEM studies [31]. In the case of the PAMC with Fe_3O_4 nanoparticles (Fig. 16g and h), the load is very homogeneously distributed. The dense micro-

---

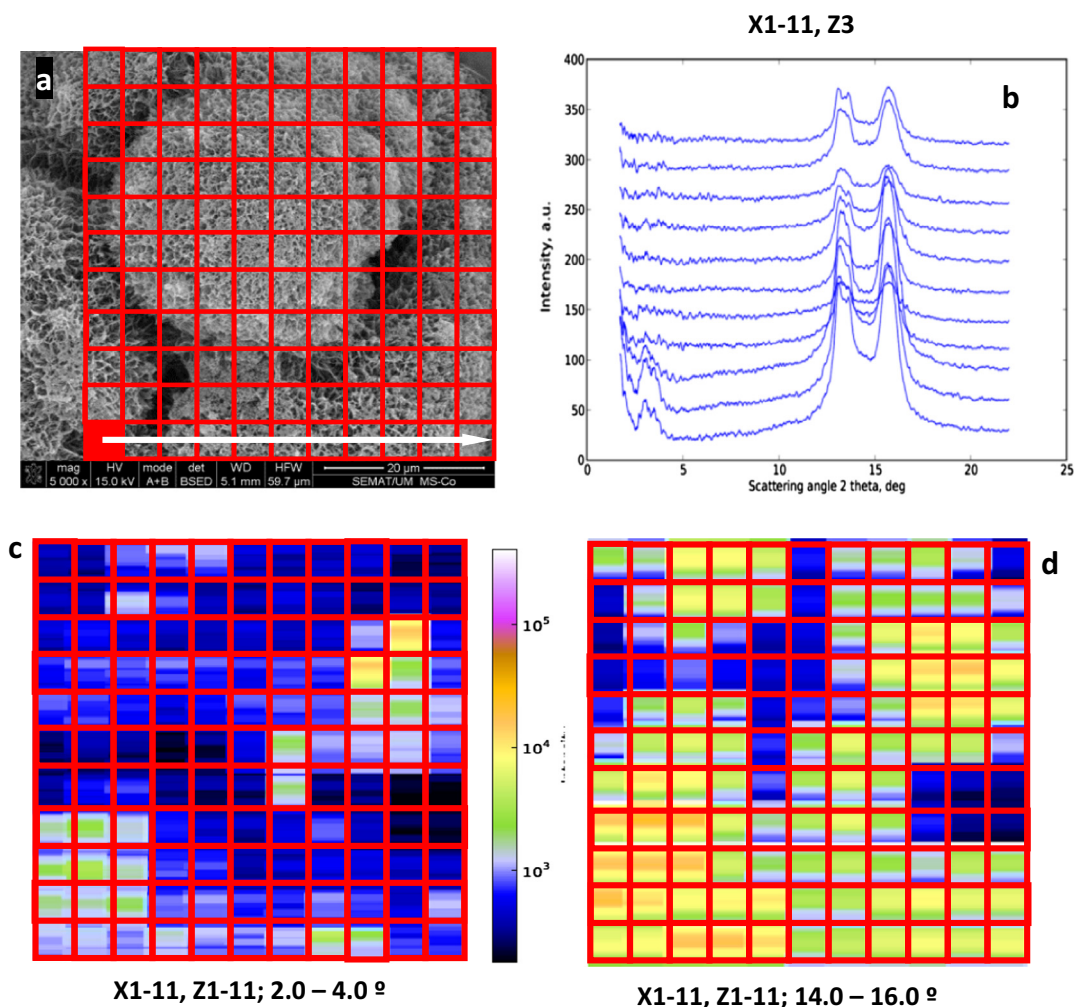[1] For interpretation of color in Fig. 15, the reader is referred to the web version of this article.

Fig. 15. Microbeam scanning of PAMC loaded with 2 wt% of NM: (a) schematics of the 11×11 grid of scanning superimposed on the SEM image of the sample; (b) the resulting WAXS linear profiles along the grid cells Z3, X1-11; (c) intensity map in the area of $2\theta = 2$–$4°$; (d) intensity map with $2\theta = 14$–$16°$.

capsule packing in the scanned area with this sample was necessary in order to obtain good mapping with the Fe_3O_4 peak at $2\theta = 20°$ (Fig. 17a). The other asterisk-marked WAXS peaks in Fig. 17a shows the WAXS reflections used for mapping the load gradients in Fig. 16, namely: $2\theta = 17°$ for GR, $25°$ for Al and the already mentioned $0\,0\,1$ basal peak of MMT at $2\theta = 2$–$4°$. The matrix PA6 peak used for mapping was the one at $2\theta = 13.4°$ related to the α $(2\,0\,0)$ plane.

The intensity maps in Figs. 15c and d and 16 can be used to select the points of interest where the nanostructure of the loaded PAMC needs to be quantified. Fig. 17b shows the linear WAXS patterns in selected grid points for all of the loaded PAMC studied. They can be deconvoluted by peak fitting which will produce data about the crystallinity index x_c, the polymorph content α/γ, and the unit cell parameters d_{hkl} for the particular grid point (Table 6).

The sample grid points in Table 6 and Fig. 17b are selected in a way that the respective load concentration is maximal so as to reveal better its influence on the nanostructure of the neighboring PA6 shell material. It can be seen that the two MMT clays increase notably the α/γ ratio as compared to the neat PA6 of the empty PAMC. The effect of GR is similar but slightly weaker. Interestingly, both MMT clays and GR possess layered structure, which may be a possible explanation of the higher α-PA6 content. Moreover, the organically-treated MMT clays are the only loads soluble in the AAP reaction medium. The two particulate loads Al and Fe_3O_4 do not produce significant change of this parameter. It seems also that the presence of GR and Fe_3O_4 load particles tends to decrease locally the crystallinity index x_c of PA6 shell. The different loads influence also the unit cell parameters d_{hkl}, the tendency toward increase being the strongest in PAMC with GR loads. It can be therefore concluded that scanning monolayers of powdered hybrid polymer materials with high flux X-ray microbeam could provide useful information about the shape and size of the microcapsules and of the embedded load particles, combined with crystallographic data in each 5×5 µm domain of the sample grid.
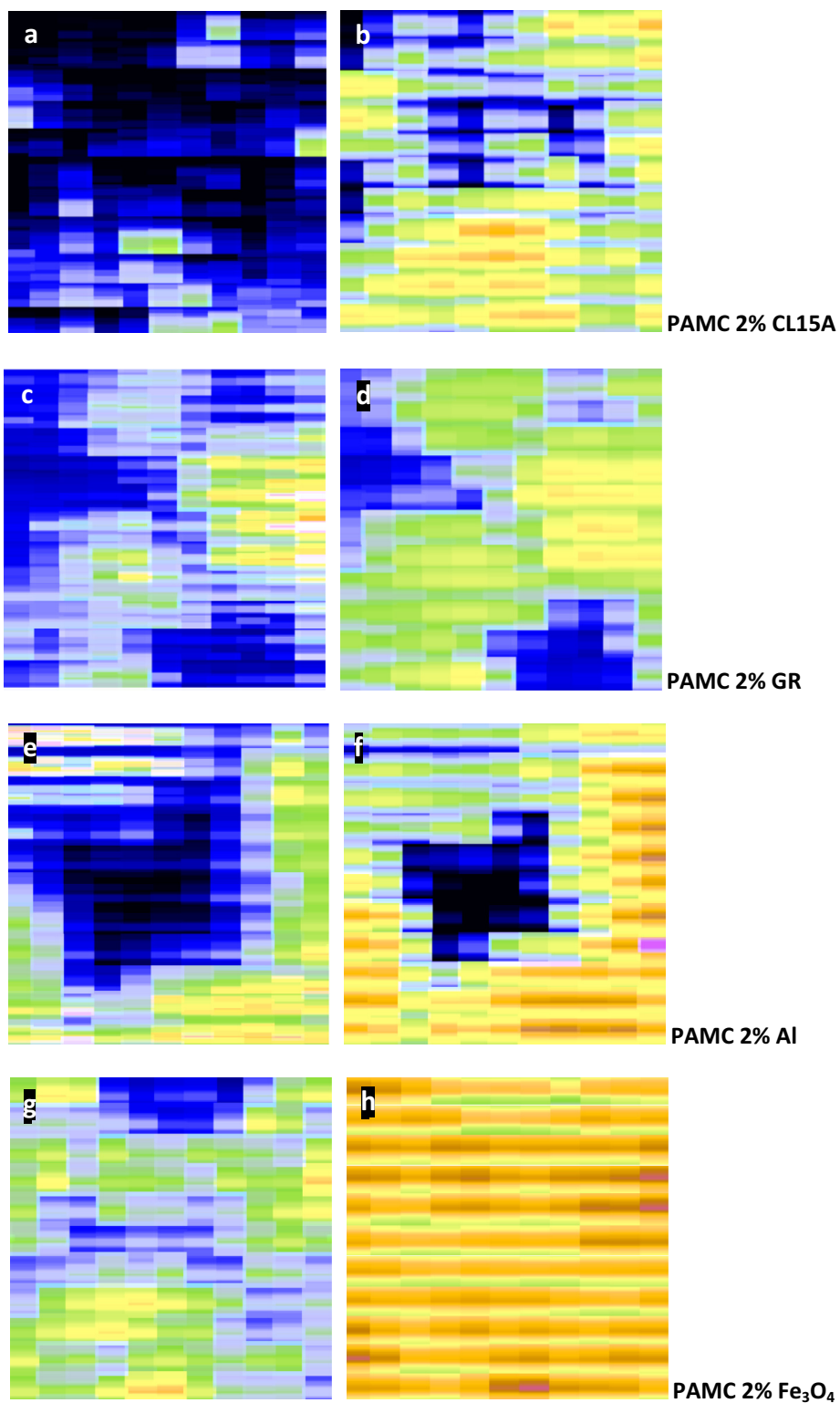
Fig. 16. Microbeam scanning of PAMC loaded with 2 wt% of various loads. The phase contrast in the images of the left column is produced on the basis of a selected WAXS peak of the load particles. The phase contrast in the right column images is based on the intensity of the PA6 matrix. For more details see the text and Fig. 17a.
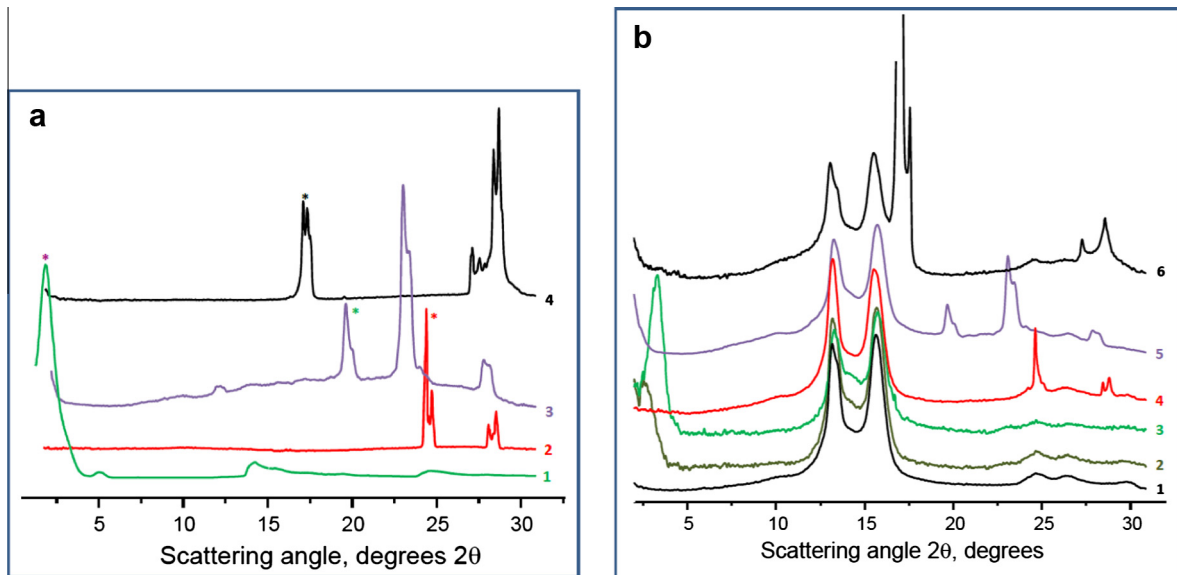
Fig. 17. Linear WAXS profiles obtained from integration of selected WAXS patterns. (a) neat load materials: 1 – CL15A; 2 – Al; 3 – Fe$_3$O$_4$; 4 – GR; (b) patterns in certain grid points showing both load and PA6 shell peaks of: 1 – empty PAMC; 2 – CL15A (Z7, X11); 3 – NM (Z9,X10); 4 – Al (Z4, X11); 5 – F$_e$3O$_4$ (Z8, X11); GR (Z7, X11).

Table 6
Nanostructure parameters extracted in selected XZ points of the sample grid for loaded PAMC.

Sample designation	α (%)	γ (%)	x_c (%)	α/γ	$d_{\alpha(200)}$ (Å)	$d_{\alpha(002)/(202)}$ (Å)	$d_{\gamma(001)}$ (Å)	$d_{\gamma(200)}$ (Å)
PAMC	38.0	17.2	55.2	2.2	4.20	3.55	4.13	3.80
PAMC/NM (Z9; X10)	42.7	10.6	53.3	4.0	4.19	3.53	3.95	3.78
PAMC/CL15A (Z7; X11)	45.7	10.8	56.5	4.2	4.21	3.54	4.03	3.91
PAMC/Al (Z4; X11)	37.3	14.3	51.6	2.6	4.21	3.57	4.20	3.87
PAMC/Fe$_3$O$_4$ (Z8; X11)	30.9	13.3	44.2	2.3	4.18	3.54	4.14	3.85
PAMC/GR (Z7; X11)	33.4	9.2	42.6	3.6	4.26	3.57	4.25	3.95

5. Concluding remarks

This work demonstrated three different strategies for accumulation and analysis of synchrotron WAXS and SAXS data focusing on their application to multicomponent hybrid composites. The samples studied possess relatively complex but strictly controlled morphology and composition, including *in-situ* MFC produced from HDPE/PA blends and PA6 microcapsules loaded with finely dispersed inorganic components. It was possible to address phenomena of theoretical and academic interest such as transcrystallinity evolution in static or dynamic conditions in microfibril-reinforced composites, and microgradient visualization in pulverulent polymer hybrids. In both MFC and PAMC material systems comprehensive structural information could be extracted that is difficult or even impossible to obtain by other analytical methods involving much more complex and labor-consuming sample preparation. Examples are the observation of stress-induced crystallization in MFC and the composition mapping in microcapsules of 20–50 μm. The evaluation of TCL thickness based on combined WAXS and SEM data is a useful approximation to assess the structure–properties relationship in engineering materials. In principle, scattering images do not reflect the sample morphology and composition directly. However, this work shows that scanning polymer structures with micro- and possibly nanosized high flux X-ray beams can have potential for both morphology visualization and fine structure characterization. In fact, microfocus WAXS could be the most appropriate method to establish the presence and analyze characteristics of TCL, provided that production of sufficiently thin samples (similar to those for TEM) is possible. We believe that the recent tremendous progress in synchrotron X-ray hardware and software combined with the increased demand for engineering soft composite materials with strictly controlled micro- and nanostructure will motivate any future attempt to extract more and more information from the X-ray scattering patterns.

Acknowledgements

References

[1] L.A. Utracki, in: Preface to Polymer Blends Handbook, Kluver Academic Publishers, Dordrecht, 2002.
[2] L.S. Schadler, Polymer-based and polymer-filled nanocomposites, in: P.M. Ajayan, L.S. Schadler, P.V. Braun (Eds.), Nanocomposite Science and Technology, Wiley-VCH, Weincheim, 2003, p. 77.
[3] A.N. Wilkinson, A.J. Ryan, Polymer Processing and Structure Development, Kluver Academic Publishers, Dordrecht, 1999.
[4] G. Groeninckx, D. Dumpas, Plastic deformation mechanisms in rubber and rubber-modified thermoplastic polymers: molecular and morphological aspects, in: T. Araki, M. Shibayama, Q. Tran-Cong (Eds.), Structure and Properties of Multiphase Polymeric Materials, CRC Press, Marcel Dekker, New York, 1998, p. 21.
[5] D. Schwahn, Critical to mean field crossover in polymer blends, Adv. Polym. Sci. 183 (2005) 1–63.
[6] K. Mortensen, Small-angle X-ray and neutron scattering studies from multiphase polymers, Curr. Opin. Solid State Mater. Sci. 2 (1997) 653–660.
[7] R.J. Roe, Methods of X-ray and Neutron Scattering in Polymer Science, Oxford University Press, New York, 2000, pp. 90–128.
[8] N. Stribeck, X-ray Scattering of Soft Matter, Heidelberg, Springer-Verlag, New York, 2007.
[9] Z. Denchev, N. Dencheva, S.S. Funari, M. Motovilin, T. Schubert, N. Stribeck, Nanostructure and mechanical properties studied during dynamical straining of microfibrillar reinforced HDPE/PA blends, J. Polym. Sci., Part B: Polym. Phys. 48 (2010) 237–250.
[10] H. Masunaga, S. Sasaki, K. Tashiro, M. Hanesaka, M. Takata, K. Inoue, N. Ohta, N. Yagi, Development of synchrotron DSC/WAXD/SAXS simultaneous measurement system for polymeric materials at the BL40B2 in SPring-8 and its application to the study of crystal phase transitions of fluorine polymers, Polym. J. 39 (2007) 1281–1289.
[11] A. Sanz, A. Nogales, T.A. Ezquerra, M. Soccio, A. Munari, N. Lotti, Cold crystallization of poly(trimethylene terephthalate) as revealed by simultaneous WAXS, SAXS, and dielectric spectroscopy, Macromolecules 43 (2) (2010) 671–679.
[12] C. Álvarez, I. Šics, A. Nogales, Z. Denchev, S.S. Funari, T.A. Ezquerra, Structure-dynamics relationship in crystallizing poly(ethylene terephthalate) as revealed by time-resolved X-ray and dielectric methods, Polymer 45 (2004) 3953–3959.
[13] R.J. Davies, C. Riekel, J.A. Bennett, S.J. Eichhorn, R.J. Young, Probing the internal geometry of a woven composite during deformation using an X-ray microdiffraction imaging technique, Appl. Phys. Lett. 91 (2007) 044102.
[14] M. Schwartz, Composite Materials Handbook, McGraw-Hill, New York, 1984. p.23.
[15] M. Evstatiev, S. Fakirov, Microfibrillar reinforcement of polymer blends, Polymer 33 (1992) 877–880.
[16] M. Evstatiev, S. Fakirov, J.M. Schultz, Microfibrillar reinforced composite from drawn poly(ethylene terephthalate)/nylon-6 blend, Polymer 34 (1993) 4669–4679.
[17] D.W. Schaefer, R.S. Justice, How nano are nanocomposites?, Macromolecules 40 (2007) 8501–9517
[18] S. Fakirov, M. Evstatiev, K. Friedrich, Nanostructured polymer composites from polymer blends: morphology and mechanical properties, in: S. Fakirov (Ed.), Handbook of Thermoplastic Polyesters, Wiley-VCH, Weincheim, 2002, pp. 1093–1132.
[19] C. Vasiliu-Oprea, F. Dan, On the relation between synthesis parameters and morphology of anionic polycaproamide obtained in organic media. I. Influence of the $Na[O(CH_2)_2OCH_3]_2AlH$/isophorone diisocyanate catalytic system, J. Appl. Polym. Sci. 62 (1996) 1517–1527.
[20] D. Suteu, D. Bilba, F. Dan, Synthesis and characterization of polyamide powders for sorption of reactive dyes from aqueous solutions, J. Appl. Polym. Sci. 105 (2007) 1833–1843.
[21] L. Ricco, O. Monticelli, S. Russo, A. Paglianti, A. Mariani, Fast-activated anionic polymerization of ε-caprolactam in suspension, 1. Role of the continuous phase on characteristics and properties of powdered PA6, Macromol. Chem. Phys. 203 (2002) 1436–1444.
[22] N. Barhoumi, A. Maazouz, M. Jaziri, R. Abdelhedi, Polyamide from lactams by reactive rotational molding via anionic ring-opening polymerization: optimization of processing parameters, eXPRESS Polym. Lett. 7 (2013) 76–87.
[23] J. Hu, S.J. Li, B.L. Liu, Properties of immobilized pepsin on modified PMMA microspheres, Biotechnol. J. 1 (2006) 75–79.
[24] E.V. Skorb, H. Möhwald, Dynamic interfaces for responsive encapsulation systems, Adv. Mater. 25 (2013) 5029–5043.
[25] D.V. Andreeva, D.G. Gorin, H. Möhwald, G.B. Sukhorukov, Novel type of self-assembled polyamide and polyimide nanoengineered shells: fabrication of microcontainers with shielding properties, Langmuir 23 (2007) 9031–9036.
[26] J. Thevenot, H. Oliveira, O. Sandre, S. Lecommandoux, Magnetic responsive polymer composite materials, Chem. Soc. Rev. 42 (2013) 7099–7116.
[27] X. Cai, Y. Zhang, G. Wu, A novel approach to prepare $PA6/Fe_3O_4$ microspheres for protein immobilization, J. Appl. Polym. Sci. 122 (2011) 2271–2277.
[28] F. Dan, C. Vasiliu-Oprea, Anionic polymerization of caprolactam in organic media: morphological aspects, Colloid Polym. Sci. 276 (1998) 483–495.
[29] C. Vasiliu-Oprea, F. Dan, On the relation between synthesis parameters and morphology of anionic polycaproamide obtained in organic media. II. Influence of the $Na[O(CH_2)_2OCH_3]_2AlH$/aliphatic diisocyanates catalytic systems, J. Appl. Polym. Sci. 64 (1997) 2575–2583.
[30] F. Dan, C. Vasiliu-Oprea, On the relationship between synthesis parameters and morphology of the anionic polycaproamide obtained in organic media. III. Macroporous powders obtained using CO_2 and carbodiimides as activating compounds, J. Appl. Polym. Sci. 67 (1998) 231–243.
[31] N. Dencheva, Z. Denchev, S. Lanceros-Méndez, T.A. Ezquerra, One-step in-situ synthesis of polyamide microcapsules with inorganic payload and their transformation into responsive thermoplastic composite materials, Macromol. Mat. Eng. (2015), http://dx.doi.org/10.1002/mame.201500194.
[32] N. Dencheva, Z. Denchev, M.J. Oliveira, S.S. Funari, Microstructure studies of in-situ composites based on polyethylene/polyamide 12 blends, Macromolecules 43 (2010) 4715–4726.
[33] M. Motovilin, Z. Denchev, N. Dencheva, On the structure-properties relationship in montmorillonite-filled polyamide 6 nanocomposites, J. Appl. Polym. Sci. 120 (2011) 3304–3315.
[34] N. Dencheva, M.J. Oliveira, O.S. Carneiro, A.S. Pouzada, Z. Denchev, Preparation, structural development, and mechanical properties of microfibrillar composite materials based on polyethylene/polyamide 6 oriented blends, J. Appl. Polym. Sci. 115 (2010) 2918–2932.
[35] N. Stribeck, U. Nöchel, S. Funari S, T. Schubert, Tensile tests of polypropylene monitored by SAXS. Comparing the stretch-hold technique to the dynamic technique, J. Polym. Sci. Polym. Phys. 46 (2008) 721–726.
[36] A. Buffet, A. Rothkirch, R. Döhrmann, V. Körstgens, M.M. Abul Kashem, J. Perlich, et al, P03, the microfocus and nanofocus X-ray scattering (MiNaXS) beamline of the PETRA III storage ring: the microfocus end station, Synchrotron Rad. 19 (2012) 647–653.
[37] W. Ruland, X-ray determination of crystallinity and diffuse disorder scattering, Acta Cryst. 14 (1961) 1180–1185.
[38] L.E. Alexander, X-Ray Diffraction Methods in Polymer Science, Wiley, New York, 1979.
[39] S.L. Aggarwal, G.P. Tilley, Determination of crystallinity in polyethylene by X-ray diffractometer, J. Polym. Sci. 18 (1955) 17–26.
[40] S. Ran, X. Zong, D. Fang, B.S. Hsiao, B. Chu, P.M. Cunniff, R.A. Phillips, Study of the mesophase in polymeric fibers during deformation by synchrotron SAXS/WAXD, J. Mater. Sci. 36 (2001) 3071–3077.
[41] G. Kortleve, C.G. Vonk, X-ray small-angle scattering of bulk polyethylene, Kolloid-Z 225 (1968) 124–131.
[42] Z. Denchev, A. Nogales, T.A. Ezquerra, J. Fernandes-Nascimento, F.J. Baltá-Calleja, On the origin of the multiple melting behavior in poly(ethylene naphthalene 2,6-dicarboxylate): microstructural study as revealed by differential scanning calorimetry and X-ray scattering, J. Polym. Sci., Part B: Polym. Phys. 38 (2000) 1167–1182.

[43] Z. Denchev, A. Nogales, I. Šics, T.A. Ezquerra, F.J. Baltá-Calleja, Probing multiple melting behaviour in poly(ethylene naphthalene 2,6-dicarboxylate) samples with different thermal history by simultaneous WAXS and SAXS, J. Polym. Sci., Part B: Polym. Phys. 39 (2001) 881–894.

[44] W. Ruland, Evaluation of the small-angle scattering of lamellar two-phase systems by means of interface distribution functions, Colloid Polym. Sci. 256 (1978) 932–936.

[45] N. Stribeck, Extraction of domain structure information from small-angle scattering patterns of bulk materials, J. Appl. Cryst. 34 (2001) 496–503.

[46] C.G. Vonk, A SAXS study of PE fibers, using the two-dimensional correlation function, Colloid Polym. Sci. 257 (1979) 1021–1032.

[47] W. Ruland, The evaluation of the small-angle scattering of lamellar two-phase systems by means of interface distribution functions, Colloid Polym. Sci. 255 (1977) 417–427.

[48] J.P. Nunes, A.S. Pouzada, C.A. Bernardo, The use of a three-point support flexural test to predict the stiffness of anisotropic composite plates in bending, Polym. Testing 21 (2002) 27–33.

[49] M. van Duin, M. Aussems, R.J.M. Borggreve, Graft formation and chain scission in blends of polyamide-6 and-66 with maleic anhydride, J. Polym. Sci., Part A: Polym. Chem. 36 (1998) 179–188.

[50] K. Friedrich, E. Ueda, H. Kamo, M. Evstatiev, B. Krasteva, S. Fakirov, Direct electron microscopic observation of transcrystalline layers in microfibrillar reinforced polymer-polymer composites, J. Mat. Sci. 37 (2002) 4299–4305.

[51] Z.-M. Li, L. Li, K.-Z. Shen, M.-B. Yang, R. Huang, In situ poly(ethylene terephthalate) microfibers- and shear-induced non-isothermal crystallization of isotactic polypropylene by on-line small angle X-ray scattering, Polymer 46 (2005) 5358–5367.

[52] N. Dencheva, Z. Denchev, M.J. Oliveira, S.S. Funari, Relationship between crystalline structure and mechanical behavior in isotropic and oriented polyamide 6, J. Appl. Polym. Sci. 103 (2007) 2242–2252.

[53] A. Zeinolebadi, N. Stribeck, M. Ganjaee-Sari, N. Dencheva, Z. Denchev, S. Botta, Nanostructure evolution mechanisms during slow load-cycling of oriented HDPE/PA microfibrillar blends as a function of composition, Macromol. Mat. Eng. 297 (2012) 1102–1113.

[54] N. Dencheva, M.J. Oliveira, A.S. Pouzada, M. Kearns, Z. Denchev, Mechanical properties of polyamide 6 reinforced microfibrillar composites, Polym. Comp. 32 (2011) 407–417.

[55] G. Strobl, The Physics of Polymers – Concepts for Understanding their Structures and Behavior, Springer, Berlin, Germany, 2007, pp. 216–220.

[56] K.U. Claussen, T. Scheibel, H.W. Schmidt, R. Giesa, Polymer gradient materials: can Nature teach us new tricks?, Macromol Mater. Eng. 297 (2012) 938–957.

Nadya Dencheva received her Master degree in organic synthesis from the University of Chemical Technologies in Burgas, Bulgaria and her PhD in the area of polymer science and technology from the University of Minho, Portugal. She is currently a member of the Institute for Polymers and Composites (IPC-University of Minho), which is a part of the i3N Associated Laboratory, Portugal. Her research focuses on the synthesis and reactive processing of polymer hybrids and studying the structure–properties relationship in multicomponent polymer systems.

Almut Stribeck received her diploma in physics and her PhD in polymer physics from the University of Marburg, Germany. At the University of Hamburg, (Institute of Technical and Macromolecular Chemistry) she had the position of a research assistant from 1982 – 1996, assistant professor from 1996-2008, and a full professor from 2008 – 2015. In 2016 she will retire. Her research interest is scattering of soft matter and the advance of related methods. She has written a text book on X-ray scattering of soft matter.

Zlatan Denchev received his Master degree at the University of Chemical Technologies in Burgas, Bulgaria and the PhD degree from the University of Chemical Technologies and Metallurgy in Sofia, Bulgaria. In the period 1983–1992 he worked at the Scientific- Research Centre for Special Polymers as research assistant. In the period 1993–2000 he joined the Faculty of Chemistry of the University of Sofia. He specialized in the area of synchrotron radiation studies on soft matter as a visiting scientist at the Max -Planck Institute for Polymer Research in Mainz, Germany and at the department of Macromolecular Physics of CSIC, Madrid, Spain. Since 2000 he is assistant professor at the Department of Polymer Engineering of the University of Minho and member of the Institute for Polymers and Composites (IPC/i3N), Portugal. Obtained a DSci degree in 2015. His research interests include the synthesis and characterization of polymer hybrids, as well as the morphology formation and phase transitions occurring in multi- component polymer systems.